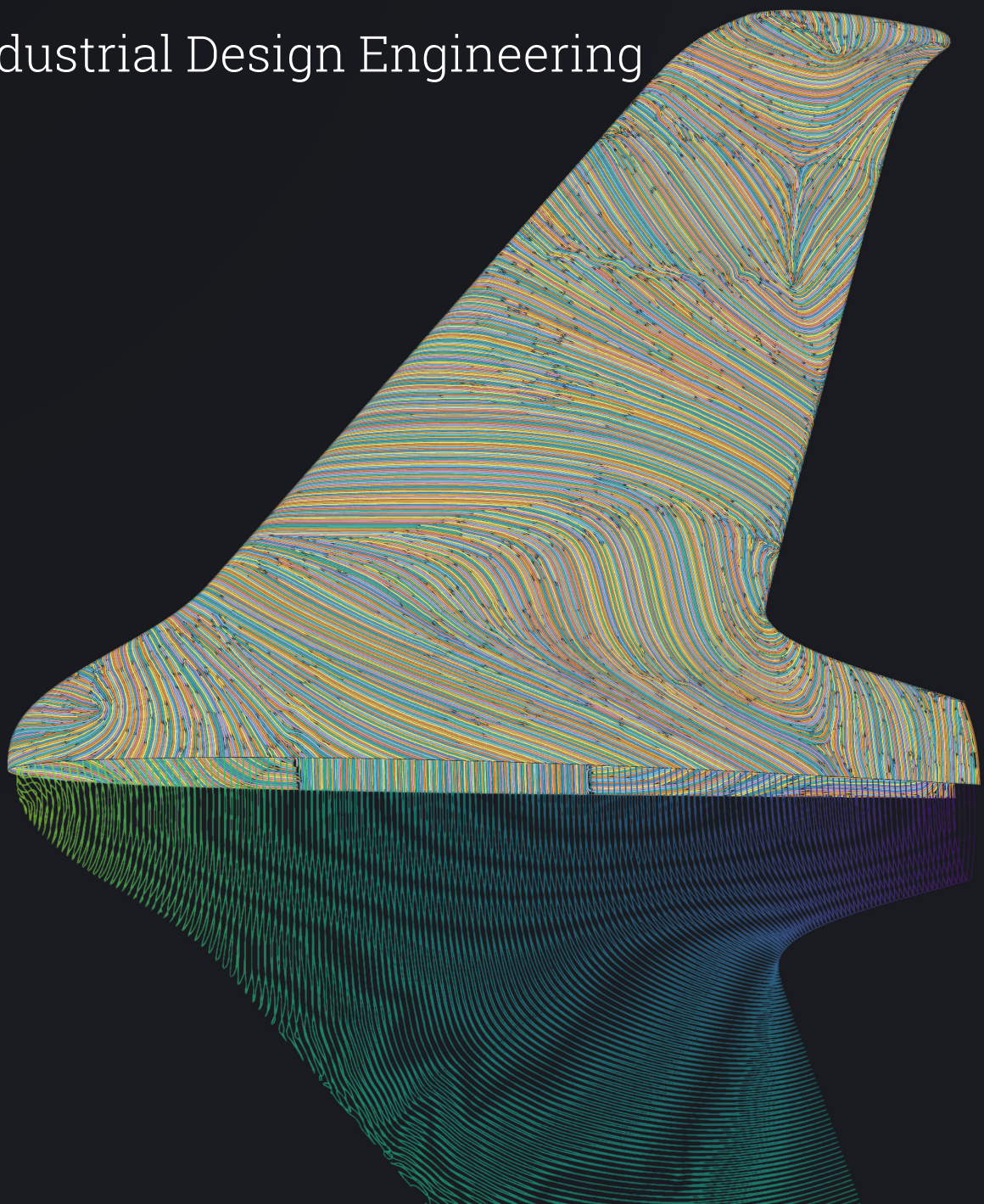
Stress-Aligned Multi-Axis Toolpaths for Thin-Walled Structures

MSc Thesis
Faculty of Industrial Design Engineering

Jun Chi

Delft University of Technology



TU Delft

STRESS-ALIGNED MULTI-AXIS TOOLPATHS FOR THIN-WALLED STRUCTURES

by

Jun Chi

in partial fulfilment of the requirements for the degree of

Master of Science

at the Delft University of Technology,
Faculty of Industrial Design Engineering

Project duration: *February* 2025 – *July* 2026

Chair: Dr. *Jun Wu*
Mentor: Dr. *Kai Wu*

TU Delft

Acknowledgements

First, I would like to thank my supervisors for their guidance throughout this project. I would not have been able to navigate a project of this scope and intensity without their encouragement, our discussions, and their critical feedback on scope and time management. The single most important lesson was to keep reminding myself that time is finite and that science advances gradually, one step at a time. Even with this awareness, I found it difficult to maintain an objective and restrained view of my own work. Learning to do so is where I have grown most as an engineer and designer during my studies at TU Delft and IDE.

I would also like to thank my friends, who encouraged me, shared fun insights, and wished me the best.

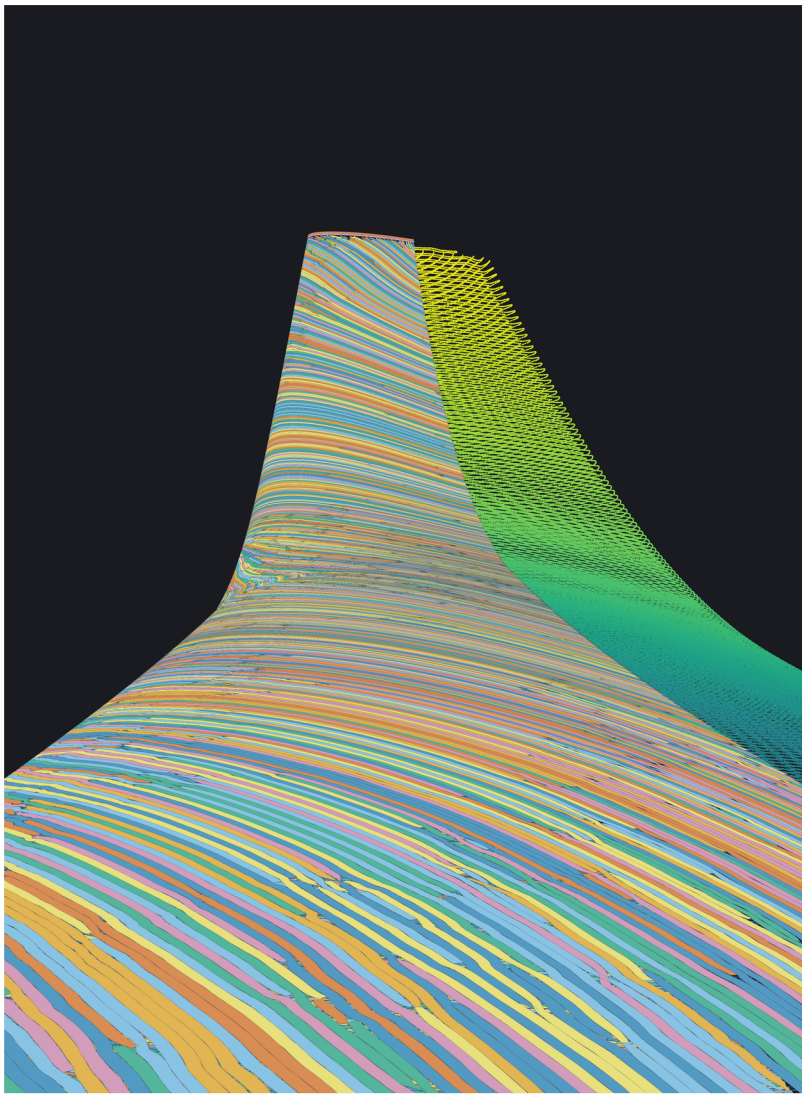
Lastly, to my family, who encouraged and supported my two-year endeavour away from home as I pursued my goals: much love, and see you soon.

Thank you and best regards,
Jun

From shell stress to an inspectable deposition proposal

The candidate sacrificial substrate is shown in context beneath the wing path layer.





The candidate substrate is shown beneath a finite-width path layer on the wing. Coloured linework outlines ordered, bed-anchored heat-method levels within the substrate. By providing a continuous deposition surface from the build plate to the curved shell, the substrate method is intended to make a separate bed-facing support structure unnecessary.

Abstract

Thin-walled products use surface geometry to combine function with low mass. Additive manufacturing can produce these shapes, but producing the shape is not equivalent to producing its intended load paths when the deposited material response is anisotropic. We investigate whether multi-axis deposition can translate a shell load case into inspectable, finite-width, stress-aligned conformal toolpath proposals before fabrication.

Short-fibre fused-filament fabrication (FFF) provides the practical case for direction-dependent deposition. The prototype links a shell stress field, shell-following layer surfaces, a spectral direction field, and finite-width path realization. Coverage, overlap, and directional error describe different geometric properties and are reported individually. We then conduct two fixed-stress evaluations: a path-dependent manufacturing-aware comparative index relating coverage shortfall, misalignment, and bead discontinuity to local demand, and a path-free comparison between one conformal material frame and prescribed planar frames. Integrating mechanics, surface geometry, path generation, and fixed-stress evaluation in one inspectable workflow is the central contribution.

Across five thin-walled shell geometries, all fifteen recorded path realizations fell below the adopted contextual reference values for coverage shortfall, overlap, and directional error at the trace-mesh resolution used in the study. A supplemental numerical check showed that exact path placement and derived measures remained sensitive to solver initialization at that resolution. For the two geometries used in the path-free material-frame comparison, the conformal frame gave a substantially lower index on the end dome, while the small wing difference was inconclusive.

These results support initial computational feasibility for generating and evaluating stress-aligned conformal paths. Physical calibration, machine planning, and coupled structural re-analysis are the next steps towards predictive and manufacturing use.

Contents

Acknowledgements i

Abstract iii

Nomenclature vi

1 Introduction 1

2 Material and mechanical preliminaries 8
2.1 Bead-scale anisotropy and the material card . . . 8
2.2 The orthotropic lamina and the cost of misalignment . . . 10
2.3 Strength scoring . . . 12
2.4 Local stationarity under fixed stress . . . 13

3 Conformal layering and stress-direction extraction 14
3.1 Stress-field source . . . 14
3.2 Reference and trace surfaces . . . 15
3.3 Reduction to a target line field . . . 15
3.4 Candidate sacrificial substrate . . . 17

4 Stress-aligned toolpath generation 18
4.1 Why a spectral phase field . . . 18
4.2 Spectral direction field construction . . . 19
4.3 Extraction and path-realization conventions . . . 22
4.4 Conditioning and verification . . . 24

5 Evaluation protocol 25
5.1 Geometric realization measures . . . 25
5.2 Manufacturing-aware comparative index . . . 26
5.2.1 Path-dependent fixed-stress evaluation . . . 26
5.2.2 Coverage and endpoint model . . . 27
5.3 Aggregation and interpretation . . . 29
5.4 Path-free material-frame comparison . . . 30
5.5 Evaluation settings and verification . . . 30

6 Results and discussion 31
6.1 Five-case comparative study . . . 31
6.2 Five-case toolpaths . . . 33
6.3 Comparison of complete path-generation pipelines . . . 34
6.4 Why stress context matters . . . 36
6.5 Solver-start sensitivity on the end dome . . . 37
6.6 Interpreting the manufacturing-aware index . . . 37
6.7 Conformal and planar material-frame sensitivity . . . 38

6.8 Computational workflow and intended use 39
6.8.1 Complex-geometry demonstrator 39
6.9 Answers to the research questions 39
6.10 Limitations 40

7 Conclusion and future work **42**
7.1 Future work 43

Bibliography **44**

Disclosure of AI use **49**

Nomenclature

Abbreviations

Abbreviation	Definition
AM	Additive Manufacturing
FE / FEM	Finite Element / Finite Element Method
FFF	Fused Filament Fabrication
FI	Failure Index (Tsai–Wu)

Symbols

Unit convention: stresses, strengths, and moduli are quoted in MPa (Pa where marked), lengths in mm, and angles in degrees unless marked rad; individual ranges are given per symbol where they matter.

Symbol	Definition	Unit
$\boldsymbol{\sigma}$	Shell stress tensor held fixed during the RQ2 path-dependent and RQ3 material-frame evaluations	MPa
$\hat{\mathbf{d}}$	Prescribed in-plane stress axis used as the target bead direction (Section 3.3)	–
$\hat{\theta}^{\mathrm{tgt}}$	Unit target line direction interpolated on the trace surface (Eq. (13))	–
θ	Fibre/bead angle (element local frame)	rad
$\mathbf{Q}$	Plane-stress lamina stiffness	MPa
E_1, E_2, G_{12}	Lamina longitudinal, transverse, and in-plane shear moduli	MPa
$\mathbf{V}_{\mathrm{ref}}, \mathbf{V}_{\mathrm{mid}}$	Vertex coordinates of the input base surface and structural midsurface	mm
$\mathbf{V}_{\mathrm{ref}}^{(f)}, \mathbf{V}_k$	Vertex coordinates of the finely remeshed base surface and conformal trace surface k	mm
t_ℓ, n_ℓ, T	Nominal layer thickness, layer count, and full shell-wall thickness $T = n_\ell t_\ell$	mm,–,mm
$\mathbf{t}, \mathbf{m}, \mathbf{n}$	Local bead tangent, in-surface transverse direction, and surface normal	–
w, p, g, o	Modelled ribbon width, centreline pitch, gap, and overlap	mm
$A, n(x)$	Evaluated trace-surface area and number of distinct modelled paths covering point x	mm^2,–
ϕ	Fraction of sixteen fixed tangent-plane ring points classified as covered by a realized path	–
$k_{\mathrm{str}}(\phi)$	Factor that reduces the in-plane strength allowables according to the local coverage fraction ϕ	–
FI	Tsai–Wu failure index $= 1/R$	–
I_{mfg}	Local manufacturing-aware index in the realized path frame, combining the fixed shell stress with coverage-dependent allowables and the open-path endpoint adjustment	–
J_{mfg}^{p99}	Physical-area 99th percentile of I_{mfg} over the evaluated conformal surface	–
ρ_h, ρ_o, ρ_d	Uncovered-area, overlap, and directional-error measures ($\rho_h \in [0,1]$; $\rho_o \geq 0$, unbounded overlap ratio; $\rho_d \in [0^\circ, 90^\circ]$)	–,–,$^\circ$
$\mathbf{X}, \mathbf{Z}$	Sets of in-plane and through-thickness strength allowables, $\{X_t, X_c, Y_t, Y_c, S_{12}\}$ and $\{Z_t, Z_c, S_{13}, S_{23}\}$	MPa

Symbol	Definition	Unit
$\boldsymbol{\psi}$	Per-vertex complex variable whose normalized argument $\arg \psi_i$ is the 2π-periodic phase used for contour extraction	–
ω_{ij}	Target phase increment assigned to mesh edge ij	rad
$\mathcal{T}_{ij}^{\omega}$	Transport operator that compares the periodic phase across edge ij after applying ω_{ij}	–
$\mathbf{W}_A$	Lumped surface-area mass matrix in the generalized phase eigenproblem	mm^2
R	Tsai–Wu strength ratio ($\mathrm{FI} = 1/R$)	–
$\mathrm{FI}_{\mathrm{conf}}^{p99}, \mathrm{FI}_{\mathrm{planar}}^{p99}$	Physical-area 99th-percentile indices for the conformal and prescribed planar material frames	–
f_{ij}^*	Tsai–Wu normal-interaction coefficients: $f_{12}^* = -\frac{1}{2}$ in both fixed-stress evaluations; f_{13}^* and f_{23}^* are inactive in the membrane-only RQ2 evaluation and set to 0 in the RQ3 material-frame comparison	–
K_t	Multiplicative bead-end stress factor applied once to all three in-plane stress components within $w/2$ (reported: $4/3$)	–
ϕ_{floor}	Coverage threshold selecting which material rule applies and clamping k_{str} (0.75)	–
b_S	Coverage-knockdown coefficient in the exponential reduction of in-plane strength allowables	–

1

Introduction

Thin-walled products often rely on their surface geometry for aerodynamics, sealing, fit, or flow, while the same shell carries load. This combination makes shells attractive for lightweight construction. Additive manufacturing (AM) can produce such complex shapes, including those generated by topology optimization (Seharing et al., 2020; Wu et al., 2018).

Producing the shape, however, is not equivalent to producing its intended load paths when the deposited material response is anisotropic. The slicing strategy sets the local bead and interlayer directions, which govern the printed response (Brenken et al., 2018; Jiang et al., 2019). We therefore ask whether the shell surface can also serve as the domain for a mechanically informed deposition pattern. We start from fixed shell geometries and stress fields obtained from a single linear-elastic structural solution for each case.

Here, direction dependent means that stiffness or strength varies with toolpath direction. Short-fibre-reinforced fused-filament fabrication (FFF) is our practical case because embedded fibres align mainly with the bead (Sun et al., 2023; Tekinalp et al., 2014). The deposited material is consequently much stiffer and stronger along the bead than across it (Ye et al., 2025). Figure 1 shows this alignment in a published single-layer short-carbon-fibre-reinforced polyamide 6 (PA6-CF) specimen. A multi-axis nozzle can follow a curved shell and deposit beads tangent to it, so deposition sets both the surface path and the local material axis. Steering that axis towards the stress direction links surface slicing to material orientation, but the paths must still maintain adequate coverage, spacing, and continuity.

We explore initial computational feasibility through a prototype workflow that translates a thin-shell load case into an inspectable, finite-width toolpath proposal. The workflow brings together the target stress direction, curved geometry, directional material response, and realized path. The proposal is an unordered set of geometric deposition paths, not machine commands. This lets us examine geometric defects and their modelled fixed-stress criterion values before fabrication while holding the shell stress field fixed.

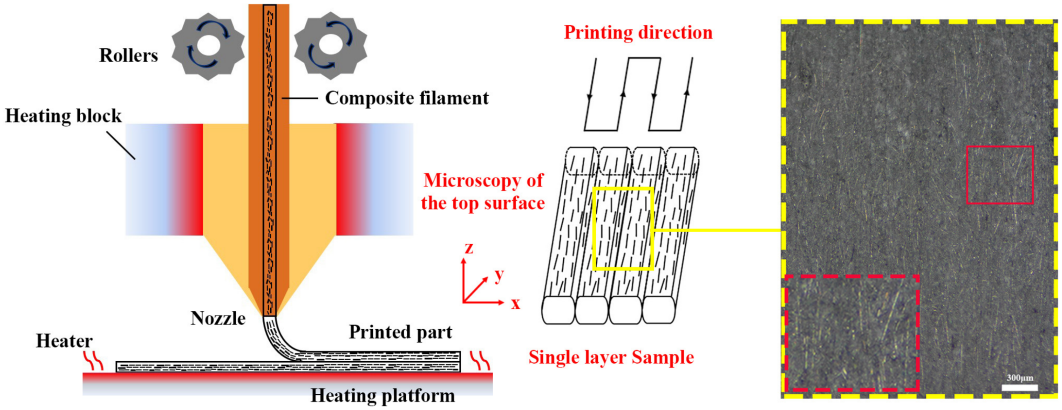


Figure 1: Short fibres in deposited PA6-CF beads align predominantly with the printing direction (reproduced from Sun et al., 2023, fig. 6, CC BY 4.0).

Short-fibre FFF is suited to this first study because cut fibres can start, stop, turn, and branch. Unlike continuous fibre, they do not require tow management or obey the same minimum-steering-radius constraints (Goh et al., 2019). Applying the workflow to another deposition process would require its material model and path constraints.

Thin-walled open shells provide a surface for conformal paths. Planar slicing confines bead directions to a fixed layer plane. That plane cannot remain tangent to every region of a curved shell, so part of the load can resolve across the weaker interlayer direction (Brenken et al., 2018). Shell-following layers reduce stair-stepping, but they reorient rather than remove interlayer interfaces (Chakraborty et al., 2008; Li et al., 2024). Constructing those layer surfaces addresses the layer geometry, but does not by itself prescribe the bead direction within each layer. Nor can one local bead direction simultaneously follow intersecting load directions. A separate path-generation step is therefore used to align the paths with the shell stress field. Figure 2 distinguishes planar layers, shell-following layer surfaces, and stress-aligned conformal paths.

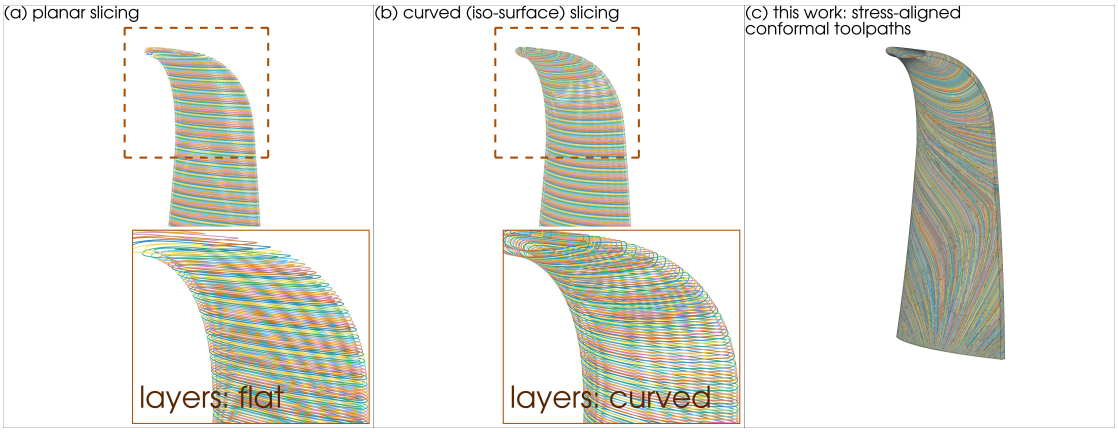


Figure 2: Planar layers, shell-following layer surfaces, and stress-aligned conformal paths on the same full-thickness wing wall, with the root on the build plate. The enlarged callouts show that planar layers cut across the winglet while shell-following layers follow it. Only panel (c) also prescribes a mechanically informed in-layer direction. Colours distinguish neighbouring paths and carry no scalar value.

Related methods differ in what they design, what they optimize, and whether they re-

solve the structural model. Principal-stress methods set material orientation from one elastic analysis. These include principal-stress-line deposition (Sales et al., 2021; Tam & Mueller, 2017), field-based continuous-fibre generation (Chen et al., 2022), stress-flow-aligned non-planar paths (Guidetti et al., 2023), stress-driven infill (G. Liu et al., 2024; T. Liu et al., 2023), and the high-density spatial fibre paths of Zhang et al. (2025). Continuous fibre-angle optimization instead re-solves the FE model at each iteration for a compliance objective (Brampton et al., 2015; Gürdal & Olmedo, 1993; Jiang et al., 2019). Compliance is the work done by the applied load and is commonly used as an inverse measure of stiffness. Strength-based steering is less common because a failure criterion can require additional analysis, whereas a compliance gradient is obtained more directly (IJsselmuiden et al., 2008). Director-field methods take an orientation field as input and optimize the following toolpath for manufacturability, as in Vector Slicer (Zmyślony et al., 2025).

This work starts from one principal-stress field obtained from a single structural solution for each case, then generates finite-width paths and evaluates their realized geometry under that fixed field.

The beads form the shell skin in this study, so complete coverage is mandatory. An uncovered region is therefore a manufacturing defect, not a loss of optional reinforcement. Published structural gains must consequently be separated by what changed. A coverage gain changes the amount of aligned fibre, whereas a direction gain holds fibre content fixed and changes only its orientation.

Controlled spacing on curved surfaces distinguishes the path-generation methods considered here. Principal-stress lines converge near stress concentrations and diverge elsewhere, so direct streamline integration produces irregular spacing. Separation-controlled tracers enforce a lower spacing bound but no upper bound, and their gap-filling paths compromise alignment (Jacquemet, 2024; G. Liu et al., 2024). Periodic-scalar methods instead construct a scalar field whose level sets target a prescribed period. This idea appears in periodic surface parameterization (Ray et al., 2006), quad-mesh generation (Bommes et al., 2009), and directional-field processing (Vaxman et al., 2016).

Two stages are relevant to the present workflow. At the field-analysis stage, Wang et al. (2026) analyse principal-stress and tensor-line structure directly on the curved domain. At the path-generation stage, Zhang et al. (2025) lift the stress axis to a sign-free direction field, solve a periodic scalar on the curved mesh, and contour it.

The present generator also operates at the path-generation stage. It uses the related surface-based generalized eigenvalue formulation of Knöppel et al. (2013, 2015) to solve a periodic phase whose level sets become paths, while a target frequency sets the nominal bead period. Discrete phase singularities account for locations where the direction field cannot close exactly. We then realize the contours as finite-width paths and evaluate the resulting geometry. The spectral mathematics is adopted from established geometric formulations; the contribution here is its integration with shell mechanics, conformal geometry, finite-width realization, and evaluation against the fixed shell stress field.

For short-fibre composites, Guo et al. (2025) combine multiscale topology optimization,

stripe-pattern dehomogenization, and robotic deposition, including a non-planar shell demonstrator. Their beads realize an optimized material distribution. Here, the beads constitute the complete thin shell, so coverage is mandatory, and defects in the realized finite-width fill are evaluated afterward against a fixed stress field.

Recent graphics methods improve the continuity and geometric feasibility of field-aligned surface fills (Chermain et al., 2025; Cocco & Chermain, 2026; Cocco et al., 2026). They target constant-thickness non-planar slicing and more continuous surface-filling toolpaths. The present work instead asks how a realized finite-width fill covers the shell and how its defects relate to a fixed local stress field. Its comparison considers complete path-generation pipelines based on streamline integration, harmonic scalar contouring, and the spectral direction field, including each pipeline's field conditioning, extraction, and finite-width realization. We use the spectral direction field for the prototype because it couples nominal bead-period targeting with directional guidance.

Zhang et al. (2025) report mechanical gains relative to their own stress-aligned but sparser prior method, but the new paths also contain more fibre, so that comparison does not isolate direction. Their field-versus-zigzag simulation is closer to a direction-only comparison, but it measures stiffness rather than strength.

A separate pure-direction result comes from continuous tow, which lies outside this study's scope: a unidirectional layup is $2.83\times$ as strong as a quasi-isotropic layup at comparable fibre content (Lupone et al., 2022). In short fibre, combined material-distribution and fibre-angle optimization gives a 12–$30\,\%$ bending-stiffness difference (Jiang et al., 2019). That range cannot be attributed to orientation alone or compared directly with the continuous-tow strength ratio.

In a membrane-dominated field with low biaxiality, one in-plane stress dominates, so the stiffness- and strength-optimal angles approach the major principal direction and re-steering gives little further gain (Gürdal & Olmedo, 1993; IJsselmuiden et al., 2008). We use the major principal axis as the mechanical reference. The five-case study also generates separate paths from the minor and locally dominant axes to test sensitivity to the chosen input direction. Chapter 6 reports their part-dependent effects.

Even after a path generator is chosen, the defects in its realized finite-width paths still require interpretation. Some prior methods already include manufacturability in their search: Vector Slicer scores gaps, overlaps, and director deviation within its parameter search, while Yang et al. constrain manufacturability during structural path optimization (Yang et al., 2025; Zmyślony et al., 2025). Here, path generation is already complete and the shell stress field is held fixed. This creates a downstream evaluation question: where do coverage shortfall, misalignment, and bead discontinuity occur relative to structural demand? The evaluation retains coverage, overlap, and alignment as separate geometric measures before relating the stress-bearing defects to the fixed shell stress field.

For the realized paths, we use two complementary evaluations. The RQ1 geometric evaluation reports coverage shortfall, overlap, and unsigned directional error separately. The RQ2 path-dependent fixed-stress evaluation relates coverage shortfall, misalignment, and bead discontinuity to a local orthotropic strength model. Its local manufacturing-aware field I_{mfg} estimates the modelled structural consequence of real-

ization defects, and J^{p99}_{mfg} is the physical-area-weighted 99th percentile of that local index. Overlap remains a separate geometric observation because the index does not model its thickness or thermal-history effects.

These path-based evaluations cannot isolate the effect of the material frame itself, because their results also depend on the realized path. We therefore add the RQ3 path-free material-frame comparison, which holds the stress field fixed and changes only the material frame between one conformal orientation and a prescribed set of planar orientations. This comparison uses prescribed material frames without introducing a realized path or structural re-solve.

Within this scope, the work addresses one overarching research question:

Overarching research question

How can a prototype workflow use the surface-following potential of multi-axis deposition to generate and evaluate finite-width, stress-aligned conformal toolpath proposals for curved thin-walled structures made from materials whose deposited properties depend on path direction?

Short-fibre FFF is the material-process case used to investigate this broader question through three operational research questions.

1. **RQ1:** How can a principal-stress field be translated into a finite-width, stress-aligned conformal toolpath on a curved thin-walled shell?
2. **RQ2:** How can coverage shortfall, misalignment, and bead discontinuity in a realized toolpath be evaluated for their modelled structural consequence under a fixed stress field?
3. **RQ3:** Under a fixed stress field, how does the predicted strength index for a conformal material frame compare with the lowest index among a prescribed set of planar material frames?

The corresponding contributions are threefold.

1. An inspectable workflow that links the principal-stress field computed for each reported case, conformal layer construction, nominal-period finite-width bead ribbons, and evaluation against the fixed shell stress field. Its path generator adapts the spectral connection-Laplacian formulation of Knöppel et al. (2015). The contribution is the integration of mechanics, geometry, path generation, and evaluation, not the underlying eigenvalue formulation. Transfer to another direction-dependent deposition process would require its material model and path constraints.
2. A path-dependent fixed-stress evaluation. We begin with the geometric defects used in fabrication-objective methods: coverage shortfall, overlap, and misalignment (Zmyślony et al., 2025). We then add bead discontinuity. The local manufacturing-aware index I_{mfg} uses an orthotropic Tsai–Wu criterion to relate the three stress-bearing defects to the fixed local shell stress; J^{p99}_{mfg} is its reported area aggregate. The index rates and localizes defects in a realized path and is separate from the generator's internal objective. The same evaluation structure could be

adapted to another direction-dependent process by replacing the maps from process defects to property reductions.

3. A five-case computational study. For each alignment input, we generate and evaluate conformal toolpaths. A complete-pipeline comparison and solver-start sensitivity examine the geometric measures. An equal-area defect-placement comparison tests the path-dependent evaluation's response to stress context, while the path-free material-frame comparison provides the second fixed-stress evaluation. We also test transfer to an optional complex-geometry demonstrator.

We combine these contributions in the computational prototype used to explore the overarching question. It produces inspectable toolpath proposals and comparative evidence before fabrication.

Figure 3 summarizes the workflow used in the report. Its solid-arrow backbone connects the common geometry-to-path stages and the available evaluation routes. The five-case study reports the three geometric measures for every generated path. A complete-pipeline comparison examines their dependence on the generator, and a solver-start sensitivity examines their dependence on numerical initialization. The equal-area defect-placement comparison examines the path-dependent index, while the path-free material-frame comparison isolates the frame change. The optional complex-geometry demonstrator uses a monobody unmanned aerial vehicle (UAV) and is treated separately in Chapter 6.

Chapter 2 introduces the material and mechanical definitions used throughout the study. Chapters 3 and 4 address RQ1 by constructing the conformal surface, extracting the stress direction, and generating the finite-width toolpath. Chapter 5 establishes the evaluation framework: its geometric measures support RQ1, its manufacturing-aware comparative index addresses RQ2, and its path-free material-frame comparison addresses RQ3. Chapter 6 applies this protocol to answer all three operational questions and assess the overarching question. The final chapter states the conclusions and the required experimental and computational extensions.

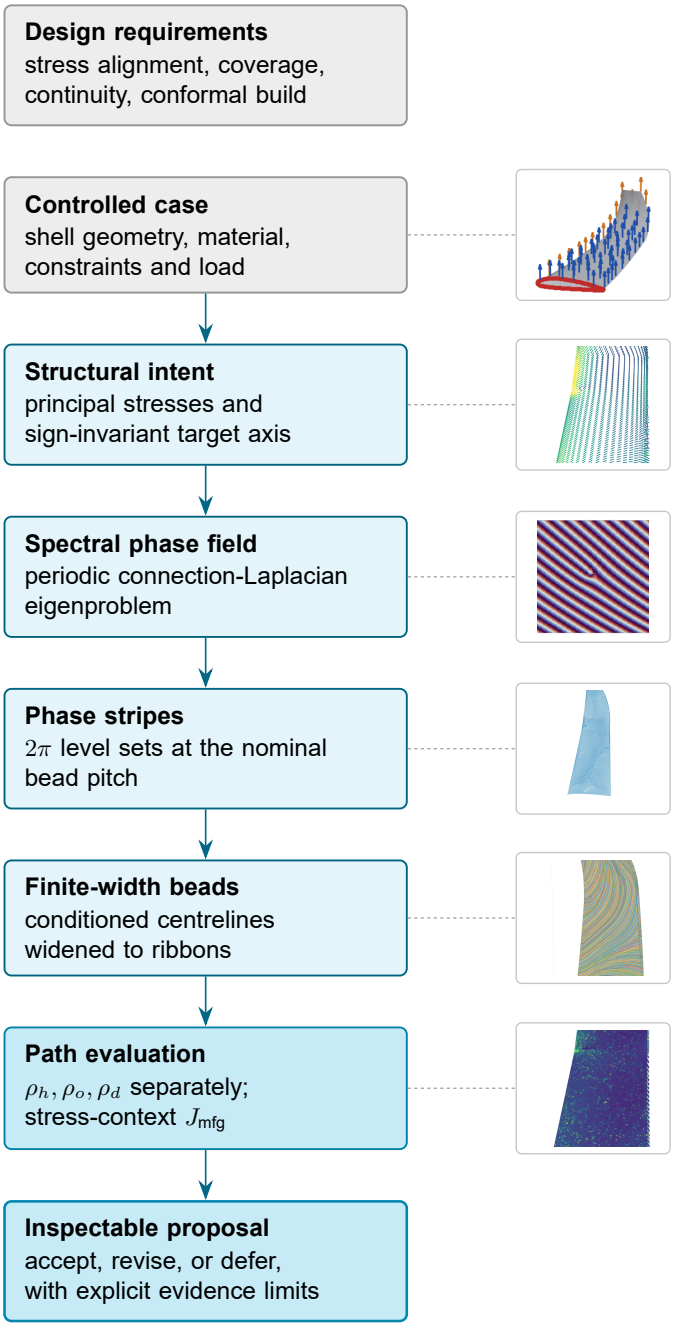


Figure 3: Computational workflow from the design requirements to an inspectable computational toolpath proposal. The solid-arrow backbone shows the common stages and available evaluation routes; the images show representative outputs from each stage.

2

Material and mechanical preliminaries

This chapter begins with bead-scale anisotropy and explains why it makes the toolpath a structural variable. We then model one deposited layer as an orthotropic lamina, a material layer with direction-dependent properties, and use that model to define the failure relations used by the manufacturing-aware comparative index. The final section gives the stationarity argument that motivates principal-stress directions.

2.1. Bead-scale anisotropy and the material card

Extruded through a converging nozzle, a carbon-fibre-filled filament emerges with its short fibres aligned to the flow, so the bead is stiff and strong along its axis and weak across it. Measured fibre-orientation distributions are far sharper than compression-moulded controls (Tekinalp et al., 2014), and reviews treat print direction as the primary determinant of the in-plane property tensor (Brenken et al., 2018; Goh et al., 2019). Each deposited bead is therefore also a reinforcement unit.

The consolidated card used throughout describes polyether ether ketone reinforced with short carbon fibres (CF–PEEK). One printed-specimen data set supplies the in-plane elastic constants and all nine tensile, compressive, and shear strength limits, conventionally called allowables, required by the fixed-stress evaluations (Ye et al., 2025). Table 1 lists the resulting computational inputs.

Each dimensional entry is multiplied by a uniform material-property knockdown factor of 0.85 and rounded as displayed in Table 1. The factor is a uniform modelling allowance for process variation, applied to a baseline already measured from printed specimens. The source Poisson ratio ν_{12} is left unscaled. The normal interaction coefficients are separate modelling assumptions, introduced in Section 2.3. The card contains the elastic constants required by the plane-stress shell model.

The card contains two distinct measures of in-plane anisotropy. The stiffness ratio $E_1/E_2 = 1.91$ sets the off-axis modulus response in Section 2.2. The in-plane tensile strength ratio $X_t/Y_t \approx 1.9$ is a separate material input. The multiaxial Tsai–Wu response

depends on the complete set of strength and interaction terms.

These ratios describe modest in-plane anisotropy in the card. A modest in-plane direction effect is therefore mechanically plausible; the corresponding sensitivity is measured in Chapter 6.

Table 1: Material card used by the plane-stress lamina and the three-dimensional strength evaluation. The displayed values are the computational inputs. Frame: 1 along the bead, 2 transverse in the layer, 3 through the layers.

Group	Constants	Values	Unit
in-plane elastic	E_1, E_2, G_{12}, ν_{12}	7420, 3882, 724, 0.29	MPa, MPa, MPa, –
along-bead strength	X_t, X_c	88, 94	MPa
transverse strength	Y_t, Y_c	46, 60	MPa
inter-layer normal	Z_t, Z_c	26, 124	MPa
shear strength	S_{12}, S_{13}, S_{23}	34, 23, 26	MPa
in-plane interaction, RQ2 path-dependent evaluation	f_{12}^*	$-1/2$	–
normal interactions, RQ3 material-frame comparison	$f_{12}^*, f_{13}^*, f_{23}^*$	$-1/2, 0, 0$	–

Inter-layer tension is the weakest normal-strength direction in the adopted card. Short fibres are predominantly bead aligned, so this response is matrix- and weld-dominated; the card uses tensile $Z_t = 26\,\text{MPa}$ and compressive $Z_c = 124\,\text{MPa}$. In the RQ2 path-dependent fixed-stress evaluation, the through-thickness stress components are zero by construction, so the in-plane allowables govern. The through-thickness entries are used only in the RQ3 path-free material-frame comparison (Section 6.7), where the fixed shell stress is resolved in a different material frame.

Feedstock class shapes the toolpath problem. Short-fibre beads can start, stop, turn, and branch without the continuity constraints of uncut continuous tow, so a layer can be filled by dense finite-width paths whose short fibres are locally aligned with each bead. Coverage and direction describe distinct properties of this realized fill, so the evaluation reports them separately.

Shell-following layer surfaces supply the geometric basis for stress-aligned conformal paths. A multi-axis machine deposits tangent to the curved layers, avoiding the staircased surface that planar slicing leaves on a curved skin. Here those layers are normal-offset copies of the known reference base surface (Chapter 3) rather than level sets of a computed build field (T. Liu et al., 2024; Zhang et al., 2022). Tool orientation toward the local surface normal is a standard assumption in multi-axis fibre deposition (Dai et al., 2018; Fang et al., 2020, 2024; Kipping & Schüppstuhl, 2023). Here, the local surface normal defines the assumed deposition-frame orientation.

Even with a prescribed finite-width path pattern, the realized deposit can still differ through variation in weld bonding, local crowding, and incomplete coverage (Brenken et al., 2018; Mehdikhani et al., 2019). This is why the evaluation in Chapter 5 acts on the finite-width toolpath rather than on the target direction field alone.

2.2. The orthotropic lamina and the cost of misalignment

In plane stress, the through-thickness stress components are negligible. We therefore model the bead as an orthotropic lamina. Direction 1 follows the bead axis, direction 2 lies transverse to it in the layer plane, and direction 3 follows the layer normal (Figure 4). In this frame, stress and strain satisfy $\boldsymbol{\sigma} = \mathbf{Q}\varepsilon$, with the standard plane-stress reduced stiffness (Barbero, 2018; Daniel & Ishai, 2006)

$$\mathbf{Q} = \begin{bmatrix} \dfrac{E_1}{1-\nu_{12}\nu_{21}} & \dfrac{\nu_{12}E_2}{1-\nu_{12}\nu_{21}} & 0 \\ \dfrac{\nu_{12}E_2}{1-\nu_{12}\nu_{21}} & \dfrac{E_2}{1-\nu_{12}\nu_{21}} & 0 \\ 0 & 0 & G_{12} \end{bmatrix}, \qquad \nu_{21} = \nu_{12}\frac{E_2}{E_1}. \tag{1}$$

Thus $\boldsymbol{\sigma}$ collects the bead-axis normal, in-layer transverse normal, and in-plane shear stresses, in that order. The strain vector uses the corresponding normal strains followed by engineering shear strain. The final relation in Eq. (1) defines the reciprocal Poisson ratio.

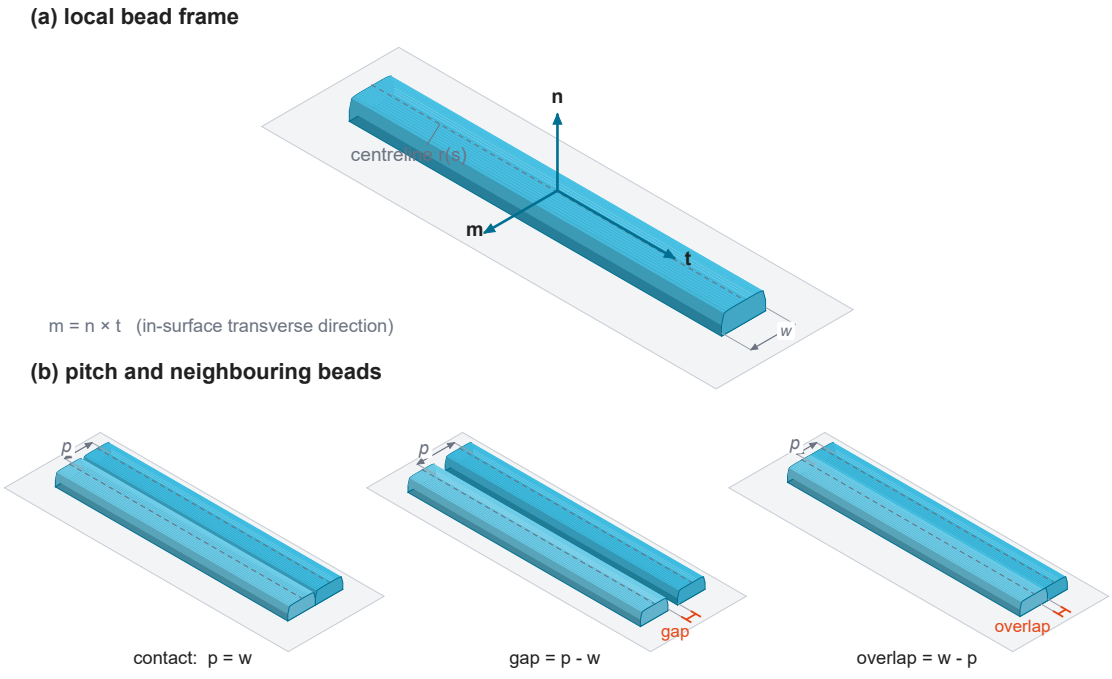


Figure 4: Explanatory geometry used to translate centrelines into finite-width beads. (a) The local tangent $\mathbf{t}$, surface normal $\mathbf{n}$, in-surface transverse direction $\mathbf{m}$, and nominal width w. (b) The pitch p produces nominal contact, a gap, or an overlap; for equal-width beads, the centreline pitch is shown by the equivalent distance between corresponding bead edges.

Figure 4(a) defines the local material frame used in this section. Figure 4(b) anticipates the finite-width coverage and overlap measures introduced in Chapter 5.

Rotating the bead axis away from the loading direction by an angle θ and applying the standard plane-stress compliance transformation gives the off-axis modulus along the

load (Barbero, 2018; Daniel & Ishai, 2006),

$$\frac{1}{E_x(\theta)} = \frac{\cos^4\theta}{E_1} + \frac{\sin^4\theta}{E_2} + \left(\frac{1}{G_{12}} - \frac{2\nu_{12}}{E_1}\right)\sin^2\theta\cos^2\theta. \tag{2}$$

This modulus is even in θ, so its expansion about alignment has no linear term,

$$\frac{1}{E_x(\theta)} = \frac{1}{E_1} + \left(\frac{1}{G_{12}} - \frac{2\nu_{12}}{E_1} - \frac{2}{E_1}\right)\theta^2 + \mathcal{O}(\theta^4), \tag{3}$$

where the final term collects fourth- and higher-order powers of θ, which is measured in radians as required by the series expansion. Only even powers appear, so the modulus is flat to first order at the aligned orientation.

For this card, $E_1/G_{12} \approx 10$. Misalignments of a few degrees therefore reduce the modulus by only a few percent (Figure 5). Farther from the stationary orientation, Eq. (2) falls steeply, reaching a minimum of $E_x/E_1 \approx 0.31$ near 49° before recovering to 0.52 at 90°. Large in-plane bead-direction errors therefore cause a substantial modulus reduction.

The geometric aggregate ρ_d, defined in Chapter 5, reports the mean angular error of the realized paths. The path-dependent fixed-stress evaluation resolves the stress at each point in the realized bead frame, so it carries the physical effect of the local angle. Section 6.7 evaluates the distinct coordinate-frame effect. The conformal frame follows the local shell normal, whereas a planar material frame uses a fixed layer normal. Expressing the same shell stress in the two coordinate systems can therefore create a component along material direction 3 in the planar frame.

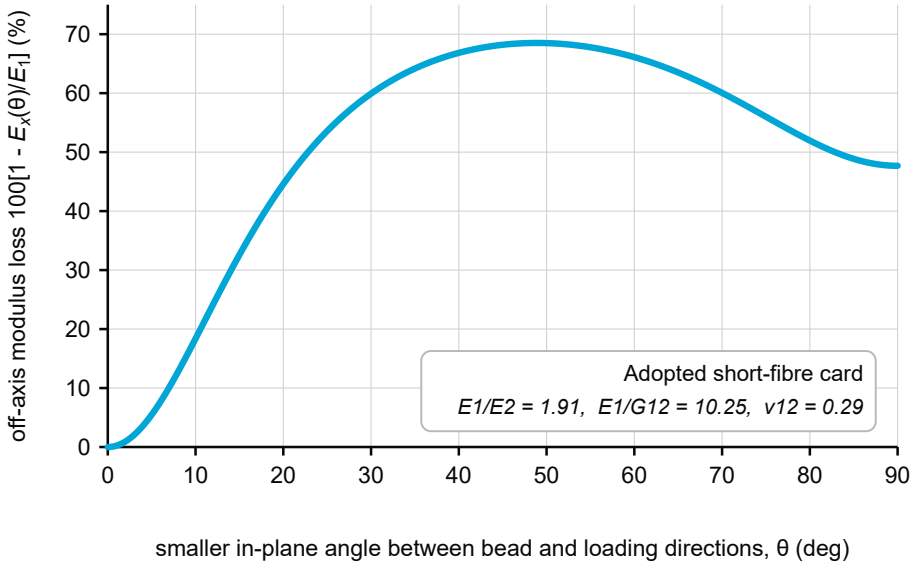


Figure 5: Off-axis modulus loss $100[1 - E_x(\theta)/E_1]$ from Eq. (2) as the smaller in-plane angle between the bead direction and the loading direction increases from 0° to 90°. The non-monotonic curve reflects the adopted short-fibre card's $G_{12} = 724$ MPa in-plane shear modulus. Strength response is evaluated separately with the Tsai–Wu criterion.

A complete conformal stack would require classical laminate theory, which assembles rotated lamina stiffnesses into membrane, coupling, and bending matrices (Barbero,

2018; Daniel & Ishai, 2006). For the fixed-stress comparisons, the study retains the membrane field from a homogeneous isotropic shell at the full modelled wall thickness and changes only the local material frame used for scoring. The same fixed shell stress field is used in the two strength evaluations described below.

2.3. Strength scoring

Both reported fixed-stress evaluations use one three-dimensional orthotropic Tsai–Wu criterion (Tsai & Wu, 1971). In the RQ2 path-dependent evaluation, the conformal material frame follows the local shell tangent plane, so the fixed membrane stress reduces the criterion to its in-plane terms. In the RQ3 path-free material-frame comparison, the planar frame instead uses a fixed layer normal, so the same fixed shell stress can have a component in the third material direction. The common three-dimensional form supports both cases.

The criterion reads $F_i\sigma_i + F_{ij}\sigma_i\sigma_j = 1$, where the F terms are coefficients constructed from the directional strength limits and repeated indices sum over the six material-frame stress components. We use this smooth failure envelope instead of mode-specific criteria such as Hashin, Puck, and LaRC (Hashin, 1980; Pinho et al., 2006; Puck & Schürmann, 2002) because it is inexpensive to evaluate at millions of points. Its linear terms retain the tension/compression asymmetry of the weak inter-layer bond.

Clarke and Hosseini (2025) showed that a Tsai–Wu surface calibrated to FFF can predict printed-polymer yield. This supports the use of Tsai–Wu as the failure-envelope form. The present coefficients come from the computational card in Table 1 and are used comparatively. The polynomial envelope returns one utilization value rather than identifying a fibre, matrix, or interface failure mode.

We report the *strength ratio* R rather than the polynomial value. R is the factor by which the complete local stress must be scaled to reach the failure envelope:

$$c_2R^2 + c_1R - 1 = 0, \qquad c_2 = F_{ij}\sigma_i\sigma_j, \quad c_1 = F_i\sigma_i, \qquad \mathrm{FI} = 1/R, \tag{4}$$

where the σ_i are the six material-frame stress components, ordered as the three normal components followed by the three shear components; repeated indices are summed. The positive root defines the strength ratio, while zero stress has an unbounded strength ratio.

The coefficients follow directly from the nine allowables: $F_1 = 1/X_t - 1/X_c$ and $F_{11} = 1/(X_tX_c)$, with the same construction for directions 2 and 3. The shear coefficients are $F_{44} = 1/S_{23}^2$, $F_{55} = 1/S_{13}^2$, and $F_{66} = 1/S_{12}^2$.

The adopted card does not provide the three independent normal interactions. Both evaluations use the conventional in-plane choice $F_{12} = f_{12}^*\sqrt{F_{11}F_{22}}$ with $f_{12}^* = -\frac{1}{2}$ (Daniel & Ishai, 2006; Tsai & Hahn, 1980). The out-of-plane interaction terms are inactive in the RQ2 path-dependent evaluation because its membrane stress has $\sigma_{33} = \sigma_{13} = \sigma_{23} = 0$. The separate RQ3 material-frame comparison sets $f_{13}^* = f_{23}^* = 0$, which makes the normalized normal-stress block of the quadratic Tsai–Wu form strictly positive definite, so every nonzero normal-stress combination contributes a positive quadratic term. Its results are reported separately in Section 6.7. The reported RQ3 comparison therefore uses these two zero out-of-plane interaction coefficients.

Under proportional loading, $R = 2$ means that scaling the complete local stress vector by two reaches the adopted criterion surface. The failure index $\mathrm{FI} = 1/R$ is therefore a criterion-utilization measure. $\mathrm{FI} = 1$ marks the adopted criterion envelope.

For the path-based study, the spatial aggregate is the physical-area-weighted 99th percentile defined in Chapter 5. It is reported in the solver-start sensitivity of Section 6.5. Every geometry-and-direction input is generated and evaluated as a separate path set, so the aggregate supports a sensitivity comparison rather than a complete-laminate inference.

2.4. Local stationarity under fixed stress

For an orthotropic lamina held at a fixed local stress state, the principal axes are *stationary* orientations of the strain energy: its derivative with respect to orientation vanishes when the material axes meet a principal strain direction (Pedersen, 1989, 1990). Under isotropy, stress and strain are coaxial, meaning that they share the same principal directions, so these are also the principal-stress directions, with $\sigma_1 \geq \sigma_2$. Which stationary orientation is a minimum depends on the stress state and anisotropy (Bendsøe et al., 1994; Vannucci & Verchery, 2001). We therefore use the algebraic major, minor, and locally dominant axes as labelled inputs in a sensitivity study, not as laminate designs (Chapter 3).

Because the first derivative vanishes at a stationary orientation, a small rotation changes compliance only to second order. This provides a mechanical basis for a controlled fixed-stress evaluation based on one structural solution, particularly as the field approaches a uniaxial state. This basis applies to the fixed stress state. Replacing the isotropic stress-source material with the orthotropic evaluation card would also change the structural solution, and stiffness- and strength-favourable orientations can also differ (Gürdal & Olmedo, 1993; IJsselmuiden et al., 2008; Setoodeh et al., 2006). Quantifying these effects requires an orthotropic structural re-solve.

3

Conformal layering and stress-direction extraction

This chapter prepares the surfaces and stress directions needed to answer RQ1. The five computational study cases pair a prosthetic socket with axial force and bending, a wing with distributed lift, an inlet duct with pressure and thrust, a tail cone with torsion and bending, and an end dome with pressure. Their dimensions are collected in Table 4; constraints, load magnitudes, and wall thicknesses are collected in Table 5. For each case, we compute a linear isotropic shell stress field, offset the reference shell geometry to obtain the conformal trace surface, and reduce the signed stress field to one target line direction per surface element. The same offset construction produces a candidate sacrificial substrate that connects the open shell to the build plate, described in Section 3.4.

3.1. Stress-field source

For each case, a standard linear-elastic isotropic shell formulation combines discrete Kirchhoff triangle bending (Batoz et al., 1980) with constant-strain triangle membrane elements (Turner et al., 1956). With $E = 4.30$ GPa, $\nu = 0.39$, and the complete modelled wall thickness, its role is to supply the stress field. The solve returns the membrane force $\mathbf{N}$ and bending moment $\mathbf{M}$ per unit width; path generation and the fixed-stress evaluations use the mid-plane membrane stress $\mathbf{N}/T$, where T is the full wall thickness defined below. The orthotropic material card is applied only during the subsequent fixed-stress evaluation (Chapter 5). The two cards therefore have distinct roles: the isotropic shell supplies the fixed stress field, and the orthotropic card evaluates the candidate material frame.

For the reported cases, the prescribed loads generate the shell stress fields directly. The same reduction can accept an imported shell stress tensor after checks of its frame, units, sign convention, and mapping to the trace surface.

3.2. Reference and trace surfaces

Let $\mathbf{V}_{\mathrm{ref}}$ be the reference base surface, $t_\ell = 0.2$ mm the nominal layer thickness, n_ℓ the layer count, $T = n_\ell t_\ell$ the wall thickness, and $\mathbf{n}_{\mathrm{ref}}$ the outward vertex normal. The structural solve uses the wall midsurface $\mathbf{V}_{\mathrm{mid}}$, and the prescribed boundary conditions and loads are applied on that surface. The shell stiffness uses the full thickness T, while the path directions use the membrane result at its neutral plane.

Candidate conformal trace surfaces offset the reference surface along its vertex normals, outward at the $t_\ell = 0.2$ mm layer thickness. A fine remesh $\mathbf{V}_{\mathrm{ref}}^{(f)}$ of the same reference geometry carries the tracing, because the trace mesh must resolve the bead period while the structural solve runs on a coarser mesh. The outward normal at each fine-mesh vertex is recomputed on that fine base remesh and is denoted by the same symbol $\mathbf{n}_{\mathrm{ref}}$. The geometric construction defines the structural midsurface and candidate trace surfaces as

$$\mathbf{V}_{\mathrm{mid}} = \mathbf{V}_{\mathrm{ref}} + \tfrac{1}{2} T \mathbf{n}_{\mathrm{ref}}, \qquad \mathbf{V}_k = \mathbf{V}_{\mathrm{ref}}^{(f)} + (k+1) t_\ell \mathbf{n}_{\mathrm{ref}}, \tag{5}$$

for $k = 0, \ldots, n_\ell - 1$. Equation (5) defines all candidate trace-surface offsets. The reported calculations use the outermost candidate surface $\mathbf{V}_{n_\ell - 1}$. Major, minor, and dominant are independent direction inputs on that same surface. The configured layer count determines the shell thickness and outer offset.

Using one common trace surface isolates path generation and fixed-stress evaluation from the additional choices introduced by a complete layer stack.

Before tracing, the coarse membrane field is interpolated on the reference surface and expressed in the tangent basis of the fine trace mesh. For the five reported cases, the interpolation is applied within one connected open shell. The spatial association uses proximity. Folded or disconnected shells require an intrinsic surface association to distinguish regions that are close in space but far apart along the surface.

For a general shell recovery, the stress at signed distance ζ from the neutral plane is

$$\boldsymbol{\sigma}(\zeta) = \frac{\mathbf{N}}{T} + \frac{12\,\mathbf{M}\,\zeta}{T^3}, \tag{6}$$

where the first term is the membrane stress and the second is the linear bending variation across the wall. Path generation and both fixed-stress evaluations use the midsurface membrane stress $\boldsymbol{\sigma} = \mathbf{N}/T$ at $\zeta = 0$. Equation (6) records the bending variation needed by a future complete-layer study.

3.3. Reduction to a target line field

The generator needs one undirected axis per element, not a tensor. A line field represents this bead direction without an arrow: $\mathbf{d}$ and $-\mathbf{d}$ denote the same direction. From the in-plane symmetric stress in each element's tangent plane we form the principal values, signed and algebraically ordered $\sigma_1 \geq \sigma_2$, with orthogonal axes. Three line fields follow from the same tensor and are treated as independent sensitivity inputs:

- *major*: the axis associated with σ_1, the algebraically larger principal, everywhere;
- *minor*: the axis associated with σ_2, the algebraically smaller, everywhere; and

- *dominant*: the axis associated element by element with $\max(|\sigma_1|, |\sigma_2|)$, the direction carrying the greater principal-stress magnitude, whether in tension or in compression.

Figure 6 illustrates this element-wise reduction.

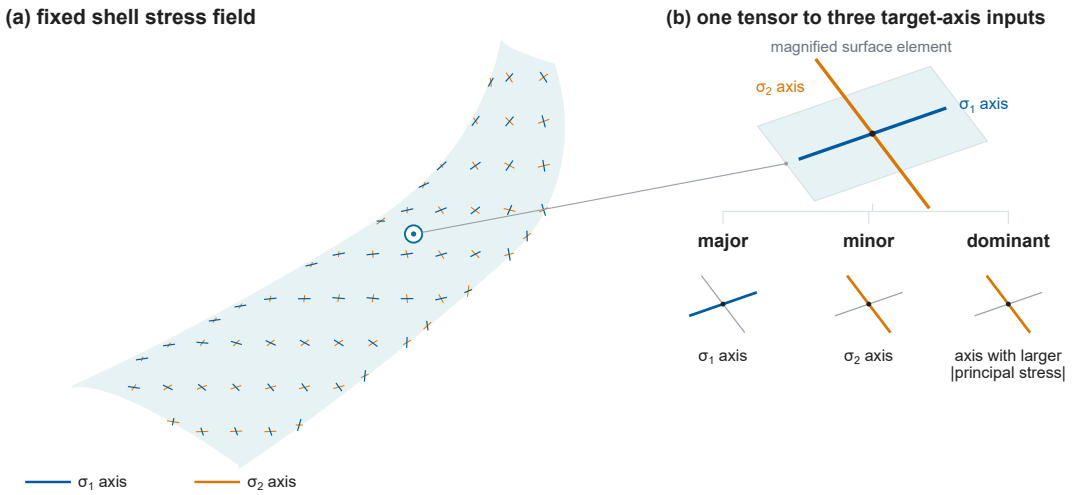


Figure 6: Reduction of the fixed shell stress field to target-axis inputs, illustrated on the wing case. (a) The principal axes are shown at reduced density. (b) For one magnified surface element, the major input follows the σ_1 axis, the minor input follows the σ_2 axis, and the dominant input follows the axis with the larger principal-stress magnitude. The three resulting target-axis fields are separate inputs to the sensitivity study.

In a mixed-sign state, the major and minor axes can be the largest tensile and the most compressive stress; in an all-tensile state, the minor axis is the smaller tensile principal. On a wrapped skin, the algebraic principal stresses σ_1 and σ_2 can exchange their magnitude ordering across loci where $|\sigma_1| = |\sigma_2|$. The algebraic and magnitude-based direction definitions can therefore assign different axes. Whichever axis is supplied becomes the input to the spectral direction field of Chapter 4. The study evaluates major, minor, and dominant as three labelled inputs. Each input produces an independently generated and evaluated path realization for the sensitivity comparison. The three-input comparison is neither an alignment ranking nor a laminate schedule. The geometric measures for these three inputs are reported in Section 6.2.

Near an equibiaxial state the two principals are close in both sign and magnitude ($\sigma_1 \approx \sigma_2$), so the stress tensor is nearly in-plane isotropic and its principal directions are ill-conditioned. They can then swing arbitrarily between neighbouring elements and produce spurious singularities, isolated points where no consistent target direction exists. Element directions are therefore weighted before averaging at the vertices by the local anisotropy

$$w_e = \frac{|\sigma_1 - \sigma_2|}{\max\big(|\sigma_1| + |\sigma_2|, 10^{-30}\,\mathrm{Pa}\big)}, \tag{7}$$

which vanishes exactly for these states. Because these are undirected line fields, neighbouring directions are sign-aligned before averaging so that opposite representations do not cancel. The element directions are then averaged at each vertex with an addi-

tional element-area weight. Near-equibiaxial elements exert almost no alignment demand and instead inherit a regularized direction from better-conditioned neighbours. At the exact equal-biaxial limit, every tangent direction is a principal direction and no unique alignment benefit exists; the regularized direction is therefore a numerical continuation through that limit, not a mechanically preferred axis. Opposite-signed states with $|\sigma_1| \approx |\sigma_2|$ are not degenerate: their axes stay well defined and retain the maximum directional weight in Eq. (7); only the dominant selection switches between the two perpendicular axes.

3.4. Candidate sacrificial substrate

Each part is an open, doubly-curved shell, so its first conformal layer has no flat base. We use the offset machinery to construct a candidate substrate beneath it. First, we extend a uniform inward per-vertex offset beyond the innermost layer, then join and cap it to form the candidate body. We extrude the bed-facing boundary to the build plate and close it with a flat annular footprint. This creates a geometric pillar with a curved substrate–part interface that matches the first structural layer. Figure 7 shows this construction for the wing case.

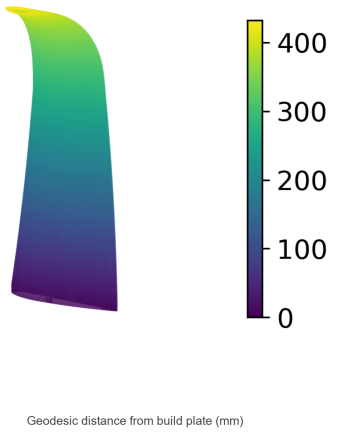


Figure 7: Candidate sacrificial substrate for the wing case. The bed-anchored conformal slices progress towards the curved substrate–part interface; colour gives geodesic distance from the build plate.

This inward substrate extension can self-intersect when its depth exceeds the local feature size, for example at a sharp trailing edge or tapering tip where opposing normals converge. A robust guard would limit the offset by the local distance to the medial axis.

To define candidate substrate slices, we use the heat method of Crane et al. (2013) to estimate geodesic distance from the build-plate boundary. Constant-distance isosurfaces of this field form the ordered substrate slices from the build plate towards the curved substrate–part interface. The structural reference shell excludes the substrate and assigns it no load.

The operations in this chapter leave each study case with a conformal trace surface and a conditioned stress-axis line field. Chapter 4 converts that pair into a periodic phase and extracts the finite-width paths evaluated in Chapter 5.

4

Stress-aligned toolpath generation

This chapter converts the conditioned stress-axis line field of Section 3.3 into finite-width surface paths at a nominal bead pitch. The generator must balance two requirements: the paths should follow the target stress direction and remain approximately evenly spaced on the curved shell.

We address these requirements with the connection-Laplacian generalized eigenvalue formulation of Knöppel et al. (2015). It produces a surface-wide periodic phase whose contours, extracted at intervals of 2π, become the path centrelines. A line direction has no arrow, so $\hat{\mathbf{d}}$ and $-\hat{\mathbf{d}}$ are equivalent. The spectral construction preserves this symmetry while balancing alignment with the target direction and spacing.

The underlying formulation is established. Our contribution is its synthesis with stress-field conditioning, conformal-shell geometry, finite-width path realization, and the evaluation protocol used in this study.

4.1. Why a spectral phase field

A principal-stress direction field is in general non-integrable: no scalar potential has a gradient parallel to it everywhere. A fibre toolpath must both target the load direction and approximately maintain the nominal bead pitch, and the two elementary constructions each satisfy only one requirement. Contouring one real harmonic scalar produces regular nested paths, but its gradient cannot follow a non-integrable direction field everywhere; Brampton et al. (2015) provide a stress-fitted example. Streamline integration, including the evenly spaced constructions of Jobard and Lefer (1997) and Jacquemet (2024), follows the field exactly but cannot guarantee gap-free coverage on a divergent field: integral curves converge and diverge, and even the evenly spaced variant leaves regions uncovered where the field spreads.

The spectral direction field couples both targets in one phase field. Its frequency targets the nominal bead pitch, while its guide field targets stress alignment. It accommodates phase-closure defects at isolated *singularities*. In the extracted contours, a singularity can appear as an interior path termination, also called a stripe dislocation. Departures from nominal spacing and local directional error can remain. The same machinery un-

derlies quad-meshing and seamless texturing on curved surfaces (Bommes et al., 2013; Vaxman et al., 2016), using only the surface's own edge lengths and angles (Crane et al., 2010; Knöppel et al., 2015). For these reasons, we use the spectral direction field to generate the paths studied here. Chapter 5 defines the separate coverage shortfall, overlap, and directional-error measures, ρ_h, ρ_o, and ρ_d. Chapter 6 applies them to paths produced by complete path-generation pipelines, including field conditioning, extraction, and finite-width realization, rather than to the mathematical generators in isolation. Figure 8 provides a qualitative comparison on one demonstration layer.

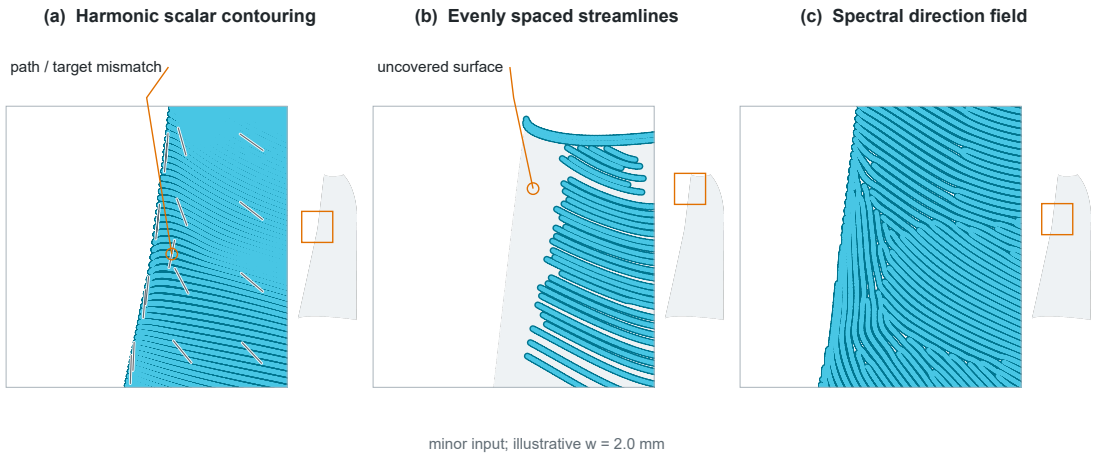


Figure 8: Qualitative diagnostic windows from one wing demonstration layer (minor input; illustrative $w = 2.0$ mm); the small silhouettes locate each window. (a) Harmonic scalar contouring shows a local departure from the direction target, which is marked by white bars. (b) Evenly spaced streamline integration leaves an uncovered region. (c) The spectral direction field distributes paths across the layer. Table 8 reports coverage, overlap, and target-specific directional error for the tested pipelines; path colour carries no scalar value.

4.2. Spectral direction field construction

We adapt the power lift, surface transport, and frequency-guided phase construction from Knöppel et al. (2015). The sequence below explains how a sign-free stress axis supplies the guide for a periodic phase and then a finite-width path.

Before the power lift, we condition the target line field to reduce sharp local changes that can cause fragmentation and additional dislocations. At each vertex, the orientation tensor $\hat{\mathbf{d}}\hat{\mathbf{d}}^{\mathsf{T}}$ is averaged over that vertex and its immediate neighbours for ten row-normalized passes. The dominant eigenvector of the final tensor is then projected into the tangent plane and renormalized. A solved phase increases along its input direction, so its level sets run across that input. We therefore use the in-surface perpendicular to the smoothed stress axis as the solver guide. This conditioned field guides generation only; directional error is evaluated against the unsmoothed transferred stress direction.

Power lift. The solver guide is a line field, so θ and $\theta + \pi$ represent the same physical axis. Doubling the angle maps these two equivalent directions to the same complex value. The solver can therefore treat the undirected axis as an ordinary single-valued field and recover the line interpretation afterward (Knöppel et al., 2013; Vaxman et al.,

2016). Per vertex, the lifted guide is

$$u_i = \exp(2\mathrm{i}\,\theta_i), \tag{8}$$

with θ_i the angle of the conditioned guide axis in vertex i's tangent frame. The principal guide half-angle is $\varphi_i^{\mathrm{tgt}} = \frac{1}{2}\arg u_i$. Here i is the imaginary unit and $\arg$ returns the complex phase angle.

Surface connection and target frequency. Guide directions at neighbouring vertices are expressed in different tangent frames. Before they can be compared, an edge-wise connection maps tangent-vector coordinates between those frames (Crane et al., 2010). Let r_{ij} denote its rotation angle, with the convention

$$\mathbf{v}_j = \mathbf{R}(r_{ij})\mathbf{v}_i, \tag{9}$$

where $\mathbf{R}(r_{ij})$ is the planar rotation through r_{ij}. $\mathbf{v}_i$ and $\mathbf{v}_j$ are the same transported tangent vector expressed in frames i and j. On a curved mesh, transport around a loop need not return a guide unchanged, so surface curvature can contribute to non-integrability.

For each directed edge $i \to j$, let α_{ij} denote that edge's angle in the source tangent frame. After transport, $\alpha_{ji}^{\rightarrow} = \alpha_{ij} + r_{ij}$. Because the guide is a line, vertex j also admits the equivalent half-angle $\varphi_j^{\mathrm{tgt}} + \pi$. The branch match selects $\widehat{\varphi}_{j|i}^{\mathrm{tgt}} \in \{\varphi_j^{\mathrm{tgt}}, \varphi_j^{\mathrm{tgt}} + \pi\}$, choosing the representative closest to the transported axis from vertex i.

After the endpoint guides are expressed on compatible branches, the solver needs a target phase increment for the edge. These increments form an edge-based quantity called a discrete one-form, with one scalar ω_{ij} assigned to each directed edge. It combines the nominal pitch with the projected guide direction:

$$\omega_{ij} = \tfrac{\ell_{ij}}{2}\big(f\cos(\varphi_i^{\mathrm{tgt}} - \alpha_{ij}) + f\cos(\widehat{\varphi}_{j|i}^{\mathrm{tgt}} - \alpha_{ji}^{\rightarrow})\big), \qquad f = \frac{2\pi}{w}, \tag{10}$$

where ℓ_{ij} is the edge length and w is the bead width. Each ω_{ij} prescribes the target phase advance across one edge at frequency $2\pi/w$. This increment sets a nominal phase frequency, not the final distance between centrelines. Curvature, singularity handling, contour extraction, and bead planning can change the spacing of the extracted and post-processed paths, so realized spacing is measured.

Connection-Laplacian eigenproblem. The prescribed edge increments cannot generally close exactly over the complete curved surface. The generalized eigenproblem combines their local residuals into one surface-wide phase mode. The implementation assembles a real symmetric quadratic form for the surface connection. Cotangent-derived edge weights set the spatial weighting, while the target-frequency increments rotate the transport along each edge:

$$\begin{aligned} E_0(\boldsymbol{\psi}) &= \sum_{ij} \widetilde{w}_{ij}\big\|\psi_i - \mathcal{T}_{ij}^{\omega}\psi_j\big\|^2 = \mathbf{q}^{\mathsf{T}}\mathbf{A}_0\,\mathbf{q}, \\ (\mathbf{A}_0 + \mathbf{D}_\varepsilon)\,\mathbf{q} &= \lambda\,\mathbf{W}_A\,\mathbf{q}, \qquad \varepsilon = 10^{-4}, \end{aligned} \tag{11}$$

where the squared norm in each edge residual measures the mismatch between neighbouring phase values after surface transport and the prescribed phase increment. The

sum over mesh edges combines these local mismatches into the surface-wide quadratic form.

Each ψ_i is the complex phase variable at vertex i, and $\mathbf{q}$ stacks the real and imaginary parts of all phase variables. The matrix $\mathbf{A}_0$ is the assembled real operator, λ is the generalized eigenvalue, and the effective edge coefficient $\widetilde{w}_{ij}$ carries the cotangent contribution used by the operator.

The transport $\mathcal{T}_{ij}^{\omega} = \mathbf{R}(-\omega_{ij})\mathbf{C}_{ij}$ combines the prescribed phase rotation with the branch flag $\mathbf{C}_{ij} \in \{\mathbf{I}, \mathrm{diag}(1,-1)\}$, where $\mathbf{I}$ is the 2×2 identity matrix. The flag matches the two vertices' equivalent line-direction branches after transport.

$\mathbf{W}_A$ is the lumped surface-area mass matrix and weights each vertex by its surrounding area. The positive diagonal stabilization is $\mathbf{D}_\varepsilon = \varepsilon \mathbf{W}_A / \mathrm{mean}[\mathrm{diag}(\mathbf{W}_A)]$. The assembled operator contains no separate $\mathbf{R}(r_{ij})$ factor: transport already informs the branch match and the edge-based increment ω_{ij}.

A shift-invert sparse eigensolve requests one mode nearest zero ($k = 1$, $\sigma = 0$). Nearby admissible modes can exist.

The returned generalized eigenvector is reshaped into one complex value per vertex and normalized pointwise. Its argument is the stripe phase. Contours taken at phase values separated by 2π define stripes extracted at the nominal pitch $p = w = 0.45$ mm and guided by the field. Because generalized eigenvectors are sign-indeterminate, ψ and $-\psi$ represent equivalent solutions of the eigenproblem. Changing the sign shifts every stripe by half a period and can therefore change which finite-width paths are extracted. Their realized spacing and alignment are evaluated from the finite-width paths rather than assumed from the prescribed phase frequency. Discrete phase-closure defects can occur on individual faces or in local face clusters where the phase fails to close. Figure 9 shows the solved phase, its level sets, and a dislocation where one stripe period terminates.

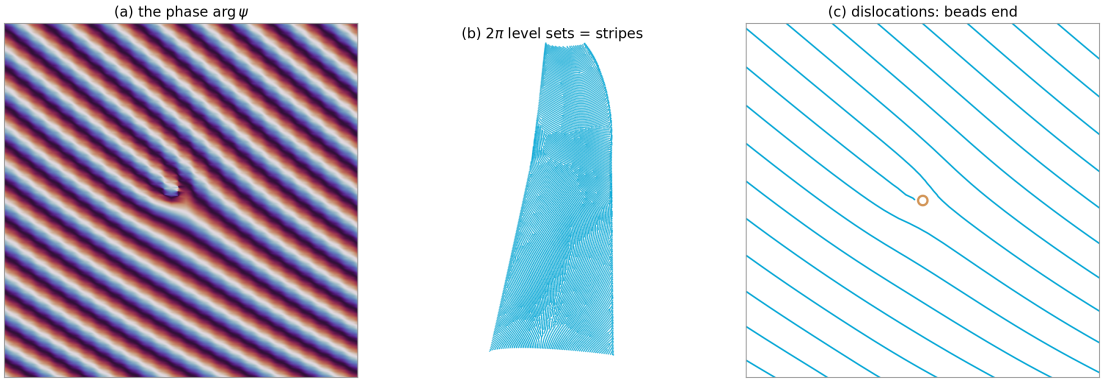


Figure 9: Stripes from a phase, on the demonstration layer of Figure 8. (a) The solved phase $\arg\psi$ targets one phase cycle per nominal bead pitch; around a dislocation, the phase accumulates a non-zero integer number of 2π turns, so one period terminates. (b) Contours separated by 2π in phase are the stripe toolpaths. (c) A window around one dislocation after extraction: one stripe ends at the dislocation, the isolated phase-closure defect that changes the local stripe count.

4.3. Extraction and path-realization conventions

Given a solved phase, we use a fixed extraction process. On each face, phase unwrapping selects equivalent corner values that differ by whole 2π periods, so the phase varies continuously along the edges. We then add the unwrapped phase changes around the triangle. Their sum can differ from zero by an integer number of full turns; the nearest integer number of 2π turns defines the face's singularity index. When the signed indices are summed over an open layer, phase changes on shared interior edges cancel. The remaining total is therefore constrained by the input field's singularities and by the net phase rotation around the layer boundary. Dislocations of opposite index can annihilate in pairs, but they cannot change this constrained total.

We locate level-set crossings on non-singular faces by linear interpolation. At a junction, straightest continuation extends both ends of a contour by selecting the unvisited outgoing edge whose unit direction has the largest dot product with the incoming unit tangent. We impose no angular rejection threshold. Singular faces are excluded, which also cuts every stripe that merely grazes an excluded triangle.

Following the singular-region treatment of the stripe-based fibre slicer of Zhang et al. (2025), we recover some fragments by clustering singular faces through shared edges and examining the level-set crossings on each cluster boundary. Free crossings on different boundary edges are paired greedily, beginning with the shortest admissible bridge. Let D be the diameter of the cluster-boundary crossings, $\hat{\mathbf{b}}$ a candidate bridge direction, and $\bar{\mathbf{d}}$ the normalized, sign-aligned mean solver guide over the cluster. The guide is perpendicular to the smoothed stress axis, while the extracted stripes run across it.

A bridge must satisfy the directional condition $|\hat{\mathbf{b}} \cdot \bar{\mathbf{d}}| \leq 0.6$. Its length must not exceed $\min\{\max(2p, 1.25D), 8p\}$. The dot-product limit keeps the bridge within 36.9° of the local stripe direction. It therefore rejects bridges that cut across neighbouring stripes and retains bridges that approximately continue a stripe. On the wing, this operation reconnects admissible raw fragments while the solved phase is held fixed. The reported geometric measures are evaluated after this reconnection.

The resulting polylines undergo two constrained-joining passes. Candidate endpoint gaps are processed shortest first within $3.5w$; the connector and the end tangents, including the reversed tangent of the second path, must pass a dot-product threshold of 0.70. The maximum lateral offset is $0.5w$, and the connector midpoint must remain at least $0.5w$ from any third path endpoint. Each endpoint is used once per accepted join. Paths shorter than $2w$ after joining are removed.

The reported path settings are collected in Table 2. In the table, width slew denotes the maximum rate at which bead width may change along a path.

Table 2: Reported numerical and geometric inputs for the spectral direction field.

Input	Relative or numerical setting	Resolved length	Role
nominal bead width and pitch	$w = p$	0.45 mm	target contour spacing
trace-mesh target edge	fixed	0.30 mm	phase-solution and contour-extraction resolution
trace-mesh diagnostic	median edge $\leq w/2$	≤ 0.225 mm	recommended-resolution check
input-direction smoothing	10 tensor-averaging passes	–	condition the solver guide
minimum retained path length	$2w$	0.90 mm	remove shorter fragments
perimeter walls	offsets $0.5w$ and $1.5w$	0.225, 0.675 mm	define the boundary deposition region
path joining	2 passes; distance $\leq 3.5w$; tangent dot product ≥ 0.70 ($\leq 45.6^\circ$)	≤ 1.575 mm	connect compatible endpoints
modelled infill-width clamp	$[0.35w, 1.25w]$	$[0.1575, 0.5625]$ mm	respond to local inter-path spacing
width-filter scale	$1.5w$	0.675 mm	regularize width variation
maximum width slew	fixed	0.225 mm/mm	limit width change along a path
squeezed-end tip width	$\max(0.05\ \mathrm{mm}, 0.4w_{\min})$	0.063 mm	taper eligible open infill ends

Two perimeter-wall centrelines are constructed at offsets $0.5w$ and $1.5w$, sampled at $0.5w$. Wall arcs shorter than $2w$ are removed. A candidate inner wall is rejected if more than half its samples fall within $0.5w$ of the preceding wall. Infill samples within w of a wall are removed; the remaining contiguous runs shorter than $2w$ are discarded. An open infill end within $2w$ of a wall is extended directly to its nearest wall sample. Serpentine routing is disabled.

Bead planning regularizes the retained infill and wall centrelines with tangent-plane-constrained λ–μ Taubin smoothing adapted from Taubin (1995). The spectral bead planner applies 24 complete λ–μ smoothing cycles. The smoothing coefficients are $\lambda = 0.5$ and $\mu = -0.53$. These path-smoothing parameters are distinct from the generalized eigenvalue used above.

At each infill sample, the raw modelled width is the distance to the nearest other infill path; perimeter walls are excluded from this spacing calculation. We clamp the resulting width sequence to $[0.35w, 1.25w]$, Gaussian-filter it using the configured $1.5w$ parameter, and limit its bidirectional change rate to 0.225 mm/mm. Walls retain the nominal width. For an endpoint of an open infill path whose planned width is below $1.5w_{\min}$, where $w_{\min} = 0.35w$, the final $1.5w$ tapers linearly to a tip width of $\max(0.05\ \mathrm{mm}, 0.4w_{\min})$. Closed paths and walls are not tapered. Perimeter-wall construction uses its own offset-loop sampling. The auxiliary resampling used only for coverage lookup in Chapter 5 does not modify the generated infill paths. These are modelled ribbon widths used in the geometric evaluation, not process-qualified extrusion widths.

4.4. Conditioning and verification

The sparse eigensolver starts from a standard-normal vector selected by an integer seed. Repeating a seed reproduces that starting vector in the same numerical environment. Path centrelines emerge only after the eigenvalue solve and contour extraction. A fixed starting vector does not remove ambiguity when nearby admissible modes form a clustered eigenspace. The comparisons retain the global sign and phase returned by each solve.

The recommended median-edge threshold $\leq w/2$ corresponds to roughly two trace-mesh edges per nominal period. The 0.30 mm trace mesh used in the study is coarser than the $w/2 = 0.225$ mm threshold. The paths and derived measures are therefore reported at this resolution. Chapter 6 examines solver-start sensitivity, while a refinement study through the $w/2$ target is needed to establish numerical convergence and quantify admissible-mode selection.

Verification on a flat constant field reproduces straight periodic contours. On curved surfaces, the computed face-index pattern provides a qualitative consistency check against the observed dislocations.

A wing check asks how much of the observed fragmentation comes from the varying stress field rather than the fixed mesh and frequency. Replacing the stress field with a uniform test field while holding the mesh and frequency fixed changes both the singular-face count and the median stripe length. Field variation therefore affects fragmentation beyond the mesh alone.

Ten tensor-averaging passes are retained as a fixed conditioning input in the reported study.

5

Evaluation protocol

This chapter defines three evaluation procedures. The first measures the completed path geometry for RQ1: finite-width ribbon coverage, finite-width ribbon overlap, and directional error are reported individually because they describe different geometric properties. The second is the path-dependent fixed-stress evaluation used for RQ2. Its local field $I_{\mathrm{mfg}}(x)$ relates coverage shortfall, misalignment, and bead discontinuity to structural demand, and its reported scalar J^{p99}_{mfg} is the physical-area 99th percentile. The third is the path-free material-frame comparison used for RQ3.

In this study, the path-dependent evaluation supports controlled comparisons under a fixed stress field. After calibration and validation on printed shells, and with structural re-solving where predictive response is required, it could provide a starting framework for quantitative structural assessment.

The five-case study reports ρ_h, ρ_o, and ρ_d for every path realization. Here, one path realization is the set of centrelines and finite-width ribbons generated for one geometry and direction input. Every geometry-and-direction input is generated and evaluated as a separate path set. The equal-area defect-placement comparison reports the mean local I_{mfg}, and the solver-start sensitivity check reports J^{p99}_{mfg}. Major, minor, and dominant inputs are evaluated independently on the same trace surface. The path-dependent and material-frame evaluations both retain the shell stress field.

5.1. Geometric realization measures

Let A be the physical area of the evaluated trace surface and let $n(x)$ be the number of distinct modelled paths whose finite-width bead ribbon covers x. The uncovered area fraction and overlap ratio are

$$\rho_h = \frac{1}{A}\int_A \mathbf{1}[n(x)=0]\,\mathrm{d}A, \qquad \rho_o = \frac{1}{A}\int_A (n(x)-1)^+\,\mathrm{d}A. \tag{12}$$

A bracketed indicator $\mathbf{1}[\cdot]$ equals one when its condition is true and zero otherwise, while $(y)^+ = \max(y,0)$ retains only positive excess coverage. A triply covered region therefore contributes twice its area to ρ_o. The finite-width ribbon estimate uses sixteen equal-area interior samples per triangle. A sample is assigned to a path when its perpendicular

distance from the local centreline is within half the modelled width; distinct covering paths define $n(x)$. Thus ρ_h and ρ_o describe the area covered by finite-width bead ribbons. The manufacturing-aware comparative index uses a different quantity, the local tangent-plane coverage fraction ϕ, defined below.

Directional error is measured along the deposited segments:

$$\rho_d = \frac{\sum_p \sum_k \frac{\ell_{pk}}{2}\left(\alpha^0_{pk} + \alpha^1_{pk}\right)}{\sum_p \sum_k \ell_{pk}}, \qquad \alpha^q_{pk} = \arccos\left|\hat{t}_{pk} \cdot \hat{\theta}^{\mathrm{tgt}}(x^q_{pk})\right|, \qquad q \in \{0,1\}. \tag{13}$$

Here ℓ_{pk} and $\hat{t}_{pk}$ are the length and unit tangent of segment k on path p, while $q \in \{0,1\}$ selects either segment end x^q_{pk}. The target is interpolated as a sign-free line on the associated surface face. The trapezoidal average therefore weights each unsigned angular deviation by deposited length. The absolute dot product makes the measure invariant to the sign of either line direction. The resulting mean is reported in degrees. Because ρ_d is a deposited-length mean, a localized directional departure can exceed the reported value. The mean is calculated only over deposited segments. An empty path realization is assigned $\rho_h = 1$, $\rho_o = 0$, and $\rho_d = 90^\circ$.

Coverage shortfall records missing deposition, overlap records repeated deposition, and directional error records deviation from the target direction. Because these are different geometric properties, they are reported individually. Path count is added in the comparison of complete path-generation pipelines and in the supplemental end-dome solver-start check. Equation (12) defines the common finite-width coverage and overlap measures, while Eq. (13) defines directional error. Following the ranges stated for typical successful Vector Slicer fills (Zmyślony et al., 2025, p. 3), we use three contextual reference values drawn from that study: $\rho_h < 5\,\%$, $\rho_o < 10\,\%$, and $\rho_d < 5^\circ$. These values provide geometric comparison context for the five-case results.

5.2. Manufacturing-aware comparative index

5.2.1. Path-dependent fixed-stress evaluation

We evaluate the local manufacturing-aware index, I_{mfg}, at every vertex of the evaluated conformal surface, with one-third of each incident triangle area assigned to that vertex. The shell analysis supplies the prescribed stress state while the realized path supplies its local tangent and defects. Consequently, I_{mfg} is the modelled local Tsai–Wu criterion-utilization value after the realized path orientation, coverage-dependent allowables, and endpoint adjustment are applied while the shell stress remains fixed. The evaluation retains the original shell stress around each defect.

This path-dependent fixed-stress evaluation uses the local tangent-plane coverage fraction ϕ and the open-path endpoint model defined below. This local lookup is separate from the finite-width ribbon coverage used to calculate ρ_h and ρ_o. The path-free RQ3 material-frame comparison is defined in Section 5.4.

At each evaluation point, the shell stress is resolved in a local material frame. The stress and structural-shell normal are supplied by the fine-surface field transfer of Section 3.2. The realized path tangent, projected into that plane, defines the first material axis. This

places the transferred stress and the realized path in one local frame. The realized tangent also defines the frame for the unmodified-property reference, even when the local coverage fraction is zero. For the membrane states used here, $\sigma_{33} = \sigma_{13} = \sigma_{23} = 0$ to numerical precision. The evaluation uses the mid-plane membrane stress, so local outer-surface bending demand would require the through-thickness recovery of Eq. (6).

To verify that coverage and endpoint adjustments enter only I_{mfg}, we use an unmodified-property reference in the realized path frame. It retains the realized orientation but excludes the endpoint adjustment, the coverage-dependent reduction in allowables, and the substitution of transverse for longitudinal allowables below the coverage threshold. Let $\boldsymbol{\sigma}^e$ denote the shell stress in this frame. The reference is

$$\mathrm{FI}_{\mathrm{plain}}(x) = \frac{1}{R(\boldsymbol{\sigma}^e(x); \mathbf{X}, \mathbf{Z})}, \tag{14}$$

Here R is the three-dimensional Tsai–Wu strength ratio of Eq. (4). The two allowable sets are

$$\mathbf{X} = \{X_t, X_c, Y_t, Y_c, S_{12}\}, \qquad \mathbf{Z} = \{Z_t, Z_c, S_{13}, S_{23}\},$$

for the in-plane and through-thickness cards, respectively. This unmodified-property quantity provides the reference for the formulation check.

5.2.2. Coverage and endpoint model

The local tangent-plane coverage fraction $\phi(x)$ is evaluated at sixteen fixed points arranged on two rings: eight equally spaced points at radius $0.6w$ and eight at radius w, where $w = 0.45$ mm is the nominal bead width. A ring point is classified as covered when the lookup finds a nearby centreline sample within a Euclidean distance of $w/2$. The same lookup rule is applied to all sixteen ring points. The rings lie in the local tangent plane and are not projected back to the curved surface. At a boundary, the ring points are neither clipped nor reweighted: all sixteen remain in the denominator and retain the same classification rule. For this lookup only, each fixed centreline is represented by auxiliary samples at a maximum arc interval of $w/4$. This auxiliary representation is used only for lookup; the generated centreline and its stored tangents remain unchanged.

The coverage-to-strength factor is

$$k_{\mathrm{str}}(\phi) = \exp[-b_S(1 - \bar{\phi})], \qquad \bar{\phi} = \max(\phi, \phi_{\mathrm{floor}}), \tag{15}$$

Here $b_S = 8$ controls how strongly incomplete local coverage reduces the in-plane allowables: at the same coverage fraction, a larger value gives a stronger reduction. The threshold $\phi_{\mathrm{floor}} = 0.75$ determines when the model switches to the transverse-only in-plane rule defined below. The exponential form follows a literature-informed porosity relation (Knudsen, 1959; Mehdikhani et al., 2019; Spriggs, 1961); b_S and ϕ_{floor} are fixed modelling inputs. The relation scales only the in-plane allowables and retains the through-thickness card unchanged.

With these sixteen ring points, the branch rule is categorical: $\phi \geq 0.75$ requires at least twelve covered points, whereas eleven or fewer select the below-threshold case. At and above the threshold, the orthotropic card is retained with its in-plane allowables scaled by $k_{\mathrm{str}}(\phi)$.

Below the coverage threshold, the in-plane stresses are reduced to their two principal normal stresses, the longitudinal tension and compression allowables are replaced by their transverse values, in-plane shear is removed, and k_{str} is held at its threshold value. The transverse lamina and through-thickness card entries are retained. The below-threshold branch represents loss of directional fibre benefit by substituting the transverse in-plane allowables within the same comparative card. For the substituted in-plane card, $F_{66} = 1/S_{12}^2 \neq 2(F_{11} - F_{12})$, so this branch remains frame-dependent. The stresses are therefore resolved in their in-plane principal frame for the quadratic contribution formed from the displayed coefficients.

The first and last points of each open path represent its bead ends; an explicitly closed loop has none. The same local lookup rule used for coverage is applied before Euclidean distance to nearby bead ends is measured. If that distance is at most $w/2$, we multiply all three in-plane stress components once by $K_t = 4/3$. Hedgepeth's nearest-neighbour broken-fibre result motivates the axial $4/3$ value (Hedgepeth, 1961). This study extends that factor to all three in-plane stress components in the comparative model. The adjustment enters I_{mfg}, while the unmodified-property reference in Eq. (14) retains the unadjusted stress.

Figure 10 summarizes these two local constructions.

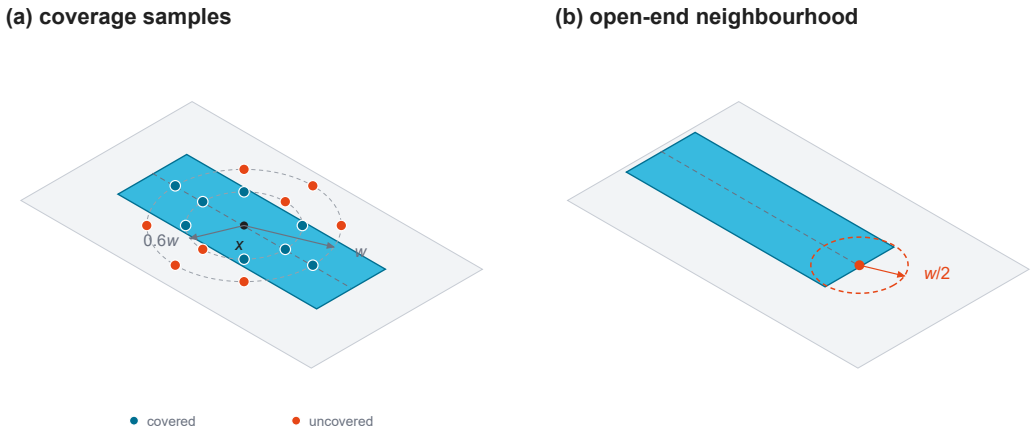


Figure 10: Local geometric constructions for the comparative defect model: sixteen tangent-plane coverage samples, eight at radius $0.6w$ and eight at w, and the $w/2$ neighbourhood around open path endpoints.

Let $\widetilde{\boldsymbol{\sigma}}$ denote the endpoint-adjusted stress and let $\widetilde{\sigma}_1^P, \widetilde{\sigma}_2^P$ be the principal values of its in-plane block. The card $\mathbf{X}_Y$ replaces X_t and X_c in $\mathbf{X}$ by Y_t and Y_c while retaining the other in-plane terms. In the second branch, the diagonal operator combines the two principal normal stresses with $\widetilde{\sigma}_{33}$ and sets in-plane shear to zero. The local manufacturing-aware field is then

$$I_{\mathrm{mfg}}(x) = \begin{cases} \dfrac{1}{R(\widetilde{\boldsymbol{\sigma}}; k_{\mathrm{str}}(\phi)\mathbf{X}, \mathbf{Z})}, & \phi \geq \phi_{\mathrm{floor}}, \\ \dfrac{1}{R\big(\mathrm{diag}(\widetilde{\sigma}_1^P, \widetilde{\sigma}_2^P, \widetilde{\sigma}_{33}); k_{\mathrm{str}}(\phi_{\mathrm{floor}})\mathbf{X}_Y, \mathbf{Z}\big)}, & \phi < \phi_{\mathrm{floor}}, \end{cases} \tag{16}$$

Overlap is reported separately. Its effects on local thickness, thermal history, and nozzle clearance lie outside the fixed-stress model.

Table 3 summarizes the resulting model analogies.

Table 3: Geometric observations and their treatment in the path-dependent fixed-stress evaluation.

Observation	Model analogue	Treatment	Origin
Coverage shortfall	missing material / porosity	$k_{\mathrm{str}}(\phi)$; below ϕ_{floor}, transverse normal allowables with no in-plane shear	literature analogy; below-threshold rule: this study
Misalignment	off-axis reinforcement	Tsai–Wu resolved in the realized path frame	established criterion
Bead discontinuity (open-path starts and stops)	local load transfer	multiplication of all three in-plane stress components by K_t within $w/2$	axial factor from literature; three-component extension: this study
Overlap	local over-deposition	reported as ρ_o; not included in I_{mfg}	not modelled

The coverage analogy follows Knudsen (1959), Mehdikhani et al. (2019), and Spriggs (1961). The material-frame criterion follows Tsai and Wu (1971). The endpoint treatment takes its axial $4/3$ value from Hedgepeth (1961). Its use as a local stress multiplier at a geometric discontinuity follows the stress-concentration convention catalogued by Pilkey and Pilkey (2008).

5.3. Aggregation and interpretation

The reported scalar is the physical-area empirical 99th percentile of I_{mfg}. For normalized lumped-area weights a_i, this area-weighted quantile is

$$J_{\mathrm{mfg}}^{p99} = \inf\left\{ z : \sum_{i:\, I_{\mathrm{mfg}\,i} \le z} a_i \ge 0.99 \right\}. \tag{17}$$

Here i indexes the evaluated surface vertices, I_{mfg_i} is the local value, the weights satisfy $\sum_i a_i = 1$, and z is the candidate threshold. The infimum selects the first threshold at which at least 99 per cent of the physical area has a value no greater than z.

The 99th percentile summarizes the upper end of the distribution without the single-point sensitivity of a raw maximum; a 95th percentile can omit a localized region covering several per cent of the surface.

J_{mfg}^{p99} is a descriptive area quantile of the comparative defect model. The value $I_{\mathrm{mfg}} = 1$ marks the adopted Tsai–Wu material-card boundary. Because even the 99th percentile can dilute a mechanism occupying less than one per cent of the surface, the Results chapter also examines a synthetic coverage defect at two equal-area placements.

Within each reported comparison, we fix the stress source, surface, material card, coverage-sampling layout, endpoint treatment, and quantile definition. The text names any quantity that changes. Paired quantile comparisons use physical-area weights and the same quantile on both sides.

5.4. Path-free material-frame comparison

For RQ3, the full-thickness isotropic shell stress field for each geometry is held fixed while only the material frame changes. The conformal frame uses the local shell normal; each planar frame uses one prescribed constant normal. In either frame, the in-plane principal-stress axis with the greater algebraic value is projected into the candidate material plane and normalized as material axis 1. The second in-plane axis completes the frame.

The same physical-area 99th-percentile Tsai–Wu index is computed for one conformal frame and thirteen planar frames. The reported planar result is the lowest value in that prescribed set. No traced path or structural re-solve enters this comparison.

The wing and end dome form a targeted two-case sensitivity within the five-case study. The pressurized dome includes the near-equibiaxial condition at its crown.

The thirteen planar normals are the sign-unique Cartesian directions with components in $\{-1, 0, 1\}$:

coordinate axes:	$[100],\ [010],\ [001],$
two nonzero components:	$[110],\ [1\bar{1}0],\ [101],$
	$[10\bar{1}],\ [011],\ [01\bar{1}],$
three nonzero components:	$[111],\ [11\bar{1}],\ [1\bar{1}1],\ [\bar{1}11].$

Each vector is normalized before use; the brackets denote components in the procedural model frame, not crystallographic indices. For the wing, x, y, and z are the chord/sweep, root-to-tip span, and lift/up coordinates. For the dome, z is the axis of revolution and x and y span the base plane. Opposite (antipodal) vectors are treated as equivalent because they define the same planar normal.

5.5. Evaluation settings and verification

The RQ2 index is evaluated with sixteen tangent-plane ring points and a $w/4$ centreline-resampling interval. Its remaining settings are $\phi_{\mathrm{floor}} = 0.75$, $b_S = 8$, $K_t = 4/3$, the common $f_{12}^{*} = -1/2$ interaction setting, and the physical-area 99th-percentile summary. The ring-point count and centreline-resampling interval are fixed numerical settings.

Two of these settings define the modelled defect response. Equation (15) uses $b_S = 8$ to map the local coverage fraction to reduced in-plane allowables. The endpoint rule uses $K_t = 4/3$ to multiply all three in-plane stress components near an open path end. Both values remain fixed across the RQ2 comparisons and define the comparative defect model.

With $k_{\mathrm{str}} = 1$ and $K_t = 1$, equality between I_{mfg} and $\mathrm{FI}_{\mathrm{plain}}$ verifies that disabling the coverage and endpoint adjustments recovers the unmodified-property Tsai–Wu evaluation in the realized path frame.

6

Results and discussion

We answer the three operational questions with the five-case study. For RQ1, we report the fifteen path realizations, compare complete path-generation pipelines for two tested combinations of geometry and alignment, and examine solver-start sensitivity on the end dome. For RQ2, we compare two equal-area artificial uncovered regions at different stress levels to establish the comparative scope of the index. For RQ3, we compare conformal and planar material frames while holding the stress field fixed. Table 2 summarizes the path settings, and Chapter 5 defines the evaluation framework. We report coverage shortfall, overlap, and directional error individually against their contextual reference values. The RQ2 comparison uses the mean local I_{mfg} within the two regions on one fixed case and stress field.

Across the tested cases, the workflow converts each computed stress line field into a nearly complete finite-width conformal fill. The complete-pipeline, equal-area defect-placement, solver-start, and material-frame comparisons delimit what those path results support.

6.1. Five-case comparative study

The dataset treats five thin-walled open shells as one comparative batch. The prosthetic socket, parametric wing, S-bend inlet duct, tail cone, and pressurized end dome span different product geometries, curvatures, and load responses. Within this comparative case series, geometry, boundary condition, load, and wall thickness vary by case, while the stress-to-path workflow, three direction inputs, bead settings, and evaluation protocol are common. Table 5 and Figure 11 summarize the prescribed computational cases introduced in Chapter 3.

Each stress field is supplied by the full-thickness isotropic shell procedure of Chapter 3, using a nominal structural mesh target of 1.0 mm. The shell solution provides the membrane field for path generation and fixed-stress evaluation. The workflow transfers that field to the conformal trace surface and represents nominal 0.45 mm bead ribbons on a 0.30 mm target trace mesh. Paths for major, minor, and dominant are generated and evaluated independently.

Table 4: Procedural geometry definitions used in the five-case study. All lengths are in millimetres.

Part	Geometry definition
prosthetic socket	length 250; terminal mean radius 65; quadratic centreline offset to 35; circumferential modulation to $\pm 13\,\%$
wing	NACA-3413-style section; root-chord scale 150; projected span approximately 360; chord tapering to 45; root trailing-edge radius 1.5; terminal cant 82°
inlet duct	length 350; radius 125; cosine centreline displacement to 60
tail cone	length 360; radius tapering from 60 to 30; quadratic centreline offset to 25
end dome	radius 175; cap at 0.995 of a quarter-circle meridian

Table 5: Prescribed reference load cases for the five geometries. Pressure fields, wing lift, and the prosthetic-socket axial patch use lumped-area weights; duct thrust is uniform over its selected ring nodes, and moments are applied as nodal force couples. The shell analysis supplies the membrane stress field for path generation and fixed-stress evaluation.

Part	Constraint	Applied load	Wall
prosthetic socket	brim ring	2400 N axial load over the distal 25 mm patch and a 20 N·m horizontal moment	3.0 mm
wing	root rib ring	area-weighted vertical lift scaled to a 30 N·m root moment	2.4 mm
inlet duct	base ring	5 kPa internal pressure and 200 N axial thrust on the upper ring	1.6 mm
tail cone	base ring	15 N·m torsion and 10 N·m bending on the tip ring	1.6 mm
end dome	base ring	0.3 MPa internal pressure	2.4 mm

The boundary and load definitions used to compute each stress field are deterministic. End rings contain nodes within 2 mm of the relevant coordinate extremum. The prosthetic-socket load covers the distal 25 mm patch; the wing root uses $y < y_{\min} + 2$ mm, and wing lift acts on upper-facing nodes with $n_z > 0.3$. Every node in a named constraint ring has all six shell degrees of freedom, three translations and three rotations, set to zero. Distributed loads use lumped surface-area weights, and the prescribed force couples have zero resultant.

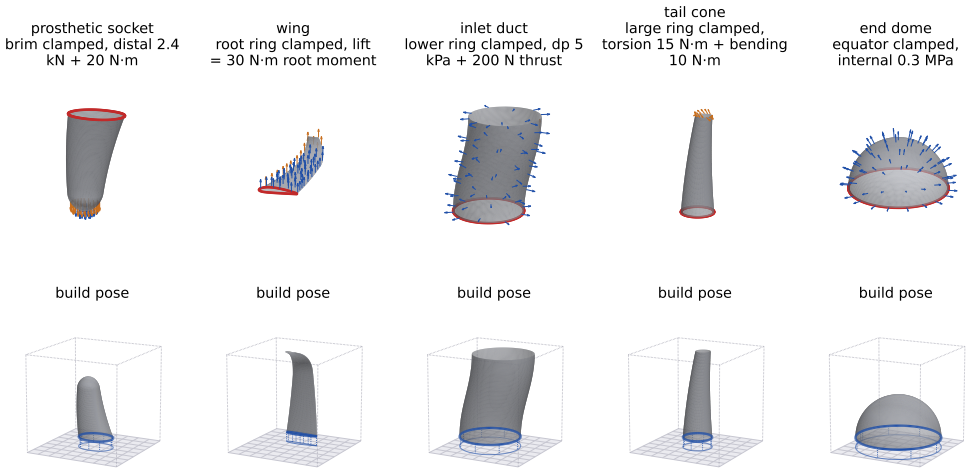


Figure 11: The five comparative geometries. The upper row shows the reference constraints and load distributions; the lower row shows the candidate build poses used in the computational study. In the raised pose shown here, the wing extends about 5 mm beyond the nominal 400 mm envelope. The inlet-duct annotation uses $\mathrm{d}p$ for the applied pressure difference; Table 5 gives the governing load and constraint wording.

6.2. Five-case toolpaths

Table 6 reports the fifteen path realizations, and Figure 12 shows a representative toolpath for each geometry. Every row reports coverage shortfall, overlap, and directional error. Here, one path realization is the complete set of finite-width paths generated for one geometry and direction input. Chapter 5 defines the three reported quantities.

Table 6: Five geometries through the stress-to-path workflow. Each row reports an independently generated and evaluated path realization. The contextual reference values are $\rho_h < 5\,\%$, $\rho_o < 10\,\%$, and $\rho_d < 5^\circ$. Section 6.5 separately examines the sensitivity of exact end-dome path placement to the eigensolver starting vector.

Part	alignment	ρ_h (%)	ρ_o (%)	ρ_d (deg)
prosthetic socket	major	1.49	4.78	3.25
	minor	0.13	0.67	1.28
	dominant	0.18	1.55	2.01
wing	major	0.25	2.36	2.16
	minor	0.37	3.68	2.14
	dominant	0.36	3.22	2.37
inlet duct	major	0.11	0.89	0.92
	minor	0.16	1.03	0.89
	dominant	0.18	1.10	1.00
tail cone	major	0.45	1.33	1.56
	minor	0.48	3.76	2.27
	dominant	0.14	1.22	1.42
end dome	major	2.28	5.29	3.74
	minor	0.93	2.41	2.01
	dominant	0.69	2.67	2.76

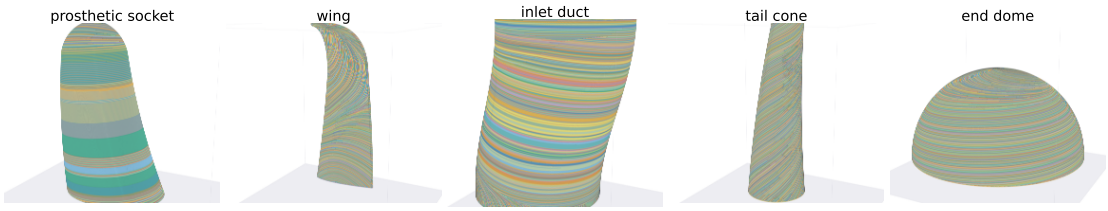


Figure 12: Stress-aligned conformal toolpaths on the five comparative geometries. Adjacency colours distinguish neighbouring beads and carry no scalar value. From left to right, the displayed inputs are minor, major, major, major, and minor; they were selected for panel legibility. Table 6 reports all three independently generated path realizations for every geometry.

At the reported trace-mesh resolution, the fifteen recorded path realizations fell below all three reference values. Among these fifteen, the maximum reported directional error is 3.74° on the end-dome major path realization, below the contextual 5° reference value. Coverage and overlap were also below their corresponding reference values for every recorded path realization. The same workflow generated these path sets for all five prescribed cases.

The end dome is the near-equibiaxial boundary case of the five. Near its crown, the two in-plane principal stresses become similar, so their associated directions become sensitive to small perturbations. This ill-conditioned region is regularized by the field-conditioning procedure described in Section 3.3. The three recorded dome paths were observed below all three reference values at the reported trace-mesh resolution. The supplemental solver-start check in Section 6.5 establishes that exact path placement remains sensitive at this resolution.

6.3. Comparison of complete path-generation pipelines

Table 8 compares three complete path-generation pipelines. For each matched geometry and direction input, the pipelines start from the same reported conformal surface, transferred field, alignment input, bead width, and metric formulas, while retaining their own field conditioning, extraction, and path-realization operations. The table therefore compares complete pipelines rather than the cited mathematical generators in isolation. Table 7 lists the fixed operating point used by each baseline pipeline.

The comparison covers the listed method–geometry–direction combinations. The dominant input on the tail cone provides the three-pipeline comparison, while the minor input on the wing compares the spectral direction field with streamline integration on a second geometry. Coverage and overlap are common geometric quantities across these rows. Directional error is target specific: harmonic scalar contouring uses its internally smoothed field, whereas the spectral direction field and streamline integration use the transferred direction target. Comparisons among the methods are therefore restricted to coverage and overlap. Each ρ_d value is a diagnostic against its pipeline's stated target.

Every reported spectral direction field row remains below the common coverage and overlap reference values and below the directional reference value for its transferred target. The tested streamline implementation follows that same target closely but leaves

Table 7: Operating points used for the two baseline pipelines in Table 8. Each baseline uses one fixed operating point and receives no case-specific optimization. Resolved lengths use $w = 0.45$ mm.

Pipeline	Field construction and tracing	Path realization
streamline integration	trace starting points at boundaries, in regions where neighbouring field directions spread apart, and on separatrices between tracing regions; no random initialization; midpoint integration step 0.225 mm; minimum clearance of 0.3825 mm from previously traced fill; termination at the boundary, previously traced fill, a degenerate or stuck trace, 4000 steps, or ten bounding-box diagonals; additional traces start at the farthest uncovered point until a $5\,\%$ internal uncovered-area target or 5000 attempts	two perimeter centrelines; remove infill from the perimeter corridor, join compatible fragments within each trace group and between the initial and gap-filling groups, and extend endpoints; modelled widths 0.1575–0.5625 mm, width-variation filter scale 0.675 mm, maximum width-change rate 0.225 mm/mm, 0.2 mm resampling interval, and ten Taubin-smoothing passes
harmonic scalar contouring	thirty sign-invariant tensor-averaging passes; alignment weight $\alpha = 4$; Dirichlet arcs at the lowest and highest $18\,\%$ of boundary projection; anisotropic harmonic scalar; contour levels redistributed from area-weighted inverse-gradient estimates in 400 bins to target a 0.3825 mm physical pitch, with the first level at half pitch and a 4000-level cap; no random initialization	no perimeter walls, joining, removal of short paths, or separate gap-filling stage; the same modelled adaptive-width range, width-variation filtering, maximum width-change rate, resampling interval, and Taubin-smoothing settings as the streamline row

Table 8: Complete path-generation pipeline results at the reported trace-mesh resolution for the tested geometry and direction-input combinations. The contextual reference values are $\rho_h < 5\,\%$, $\rho_o < 10\,\%$, and $\rho_d < 5^\circ$. Coverage and overlap use common geometric definitions. Directional error for the spectral direction field and streamline integration uses the transferred stress target; the harmonic scalar contouring result uses its internally smoothed target. “Paths” counts retained connected centreline polylines.

Case and alignment input	method	paths	ρ_h (%)	ρ_o (%)	direction target	ρ_d (deg)
wing, minor input	spectral direction field	2722	0.37	3.68	transferred stress	2.14
	streamline integration	1927	29.86	0.71	transferred stress	0.81
tail cone, dominant input	spectral direction field	1370	0.14	1.22	transferred stress	1.42
	streamline integration	938	13.35	0.98	transferred stress	0.43
	harmonic scalar contouring	1844	2.01	15.79	internal smoothed	34.52

13.35–$29.86\,\%$ of the surface uncovered. The one reported row for harmonic scalar contouring remains below the coverage reference value but exceeds the overlap reference value. Its $34.52°$ directional error also exceeds the directional reference value when judged against its own smoothed target. Because the comparison did not isolate the cause, this result characterizes only the tested implementation of harmonic scalar contouring.

The reported comparison shows why the geometric measures are reported individually. Streamline integration follows the target direction closely but leaves substantial areas uncovered. A compensatory aggregate or weighted sum could therefore allow low directional error to obscure poor coverage. Reporting ρ_h, ρ_o, and ρ_d individually keeps missing deposition, repeated deposition, and directional deviation visible.

6.4. Why stress context matters

The question is whether the same coverage defect receives a different score when it occurs under different stress demand. We test this with two artificial uncovered regions of equal area at high- and lower-stress sites on the same evaluated path realization. Each sets the local coverage fraction to $\phi = 0$ at evaluation points inside a Euclidean disc on the conformal surface. The high-stress disc has a 5.0 mm radius and is centred on the sample with the largest $\|\boldsymbol{\sigma}\|_F$. Here, $\|\boldsymbol{\sigma}\|_F$ is the Frobenius magnitude, defined as the square root of the sum of the squared stress-tensor components. We place the lower-stress centre at the sample farthest from the first centre within the lowest stress-magnitude quartile. The lower-stress disc has a radius of 6.98 mm, which makes both discrete regions occupy $0.085\,\%$ of the surface at the reported precision. Their centres are separated by at least 80 mm. This exploratory comparison applies no additional boundary or bead-endpoint exclusion.

For the capped stress-magnitude control, we multiply all six components of each stress tensor by the same positive pointwise factor. We first average the Frobenius magnitude with normalized lumped-area weights. At each point, the factor is this average divided by the local Frobenius magnitude, with a 10^{-12} denominator floor and a cap of 100. The transformation targets this common magnitude while retaining tensor directions, component signs, and biaxiality. Table 9 compares the two placements before and after the transformation.

Table 9: Equal-area artificial coverage-defect comparison on the prosthetic socket, shown for the dominant alignment. Both regions assign zero local coverage. The score is the area-weighted mean I_{mfg} over the artificial uncovered region; the stress column is the area-weighted mean Frobenius norm $\|\boldsymbol{\sigma}\|_F$ within that region.

Placement	void area (%)	mean $\|\boldsymbol{\sigma}\|_F$ (MPa)	mean I_{mfg}, original stress	mean I_{mfg}, capped magnitude control
high-stress brim site	0.085	3.4	0.27	0.18
lower-stress site	0.085	1.1	0.15	0.20

The high-stress sample lies on the constrained brim ring. With the physical stress field retained, that placement receives the larger score. Under the capped stress-magnitude

control, the two readings become similar and the small residual difference reverses. For this pair, that reduction indicates that stress magnitude is a principal contributor to the observed contrast. Other factors remain after the control: component signs and biaxiality, the different disc geometries and spatial samples, any endpoint adjustment, and any magnitude difference left by the cap. Because local coverage is zero, path-axis orientation does not enter this branch of the model.

6.5. Solver-start sensitivity on the end dome

The end dome provides a focused numerical sensitivity check because its principal directions are ill-conditioned near the equibiaxial crown. As a supplemental check, we generated major-input and minor-input paths with eigensolver-start seeds 0, 1, and 3. The integer seed changes only the standard-normal starting vector supplied to the sparse generalized eigensolver. The dome geometry, fixed shell stress field, trace mesh, target frequency, path-realization settings, and evaluation settings remain fixed. The controlled set includes only rows with identical recorded geometry, stress, mesh, eigensolver backend, and path and evaluation settings.

Table 10: Exploratory end-dome solver-start sensitivity check. The seed selects the standard-normal starting vector for the sparse eigensolver. Coverage shortfall and overlap are reported as percentages; J^{p99}_{mfg} is the same physical-area quantile used elsewhere in the path-dependent evaluation.

Input	seed	paths	ρ_h (%)	ρ_o (%)	ρ_d (deg)	J^{p99}_{mfg}
major	0	35123	2.59	9.80	5.61	1.757
major	1	9615	0.81	4.08	2.87	0.856
major	3	6269	0.62	3.34	2.51	0.829
minor	0	9629	0.40	5.14	3.80	0.869
minor	1	5809	0.29	4.08	3.10	0.867
minor	3	3261	0.19	2.87	2.63	0.576

The solver-start change produces different bead sets and different derived measures. The major-input path count spans 6269–35123, and one of its three directional-error values exceeds the contextual 5° reference value. The minor-input path count spans 3261–9629, while its three geometric results remain below all three contextual reference values. The J^{p99}_{mfg} ranges are 0.829–1.757 for the major input and 0.576–0.869 for the minor input. The check therefore shows that the eigensolve-to-extraction chain and its derived measures are sensitive to the starting vector at the reported trace resolution. The comparison is interpreted as numerical sensitivity within each direction input.

The retained diagnostics do not include phase-aligned eigenvectors, spectral gaps, or eigenpair residuals, so this check cannot assign the variation to one mechanism. Possible contributors include selection among nearby admissible modes, the arbitrary global sign or phase of the eigenvector, the under-resolved trace mesh, and poorly conditioned target directions near the dome crown. Resolving the underlying non-uniqueness and conditioning is left to future work.

6.6. Interpreting the manufacturing-aware index

The literature-informed coverage law and endpoint factor set the scale of the comparative defect model. The results therefore use the index for within-case comparison.

Physical pass–fail interpretation requires process-specific calibration.

The geometric measures and J^{p99}_{mfg} answer different questions. ρ_h, ρ_o, and ρ_d report coverage, overlap, and alignment separately. J^{p99}_{mfg} combines a realized material frame with modelled coverage and endpoint effects under a fixed stress field. Physical-area weighting prevents evaluation-mesh density from becoming an implicit weight, and the 99th percentile limits the influence of one extreme evaluation point. A very small defect may occupy too little physical area to change the global 99th percentile. The equal-area test therefore reports mean local I_{mfg} inside each artificial uncovered region, directly summarizing the response over the perturbed area.

6.7. Conformal and planar material-frame sensitivity

Table 11 reports the path-free material-frame comparison defined in Section 5.4. Within any one material frame, a larger failure index is more adverse. The table deliberately reports the lowest index among thirteen tested planar normals, rather than the root-on-bed manufacturing pose, and compares it with one conformal frame.

For the wing, the span-vertical root-on-bed frame is manufacturing-relevant because it avoids placing a broad curved skin at the bed-facing support–part interface. The minimum-index planar normal in the table is a numerical comparator. Assessing a practical build orientation also requires support-contact and surface-quality evaluation.

Table 11: Path-free comparison of conformal and planar material frames using the fixed isotropic shell stress field for each reported geometry at the finest tested structural resolution. Both columns use the same physical-area 99th-percentile Tsai–Wu definition, reference material properties, and fixed structural solution.

Part	$\mathrm{FI}^{p99}_{\mathrm{conf}}$	lowest tested $\mathrm{FI}^{p99}_{\mathrm{planar}}$	tested planar normal	FI ratio: planar/conformal
wing	0.0962	0.0930	$[100]$	0.967
end dome	0.2176	0.5236	$[101]$	2.406

The two cases give different results. On the wing, the lowest of the thirteen planar-frame values is about $3.3\,\%$ below the conformal value. On the dome, it is about 2.4 times the conformal value.

The planar value is the minimum over thirteen tested planar normals, whereas the conformal value is a single frame. The wing's small margin cannot be separated from this one-versus-thirteen asymmetry and therefore cannot establish a planar advantage. The dome contrast remains large within the same asymmetric comparison.

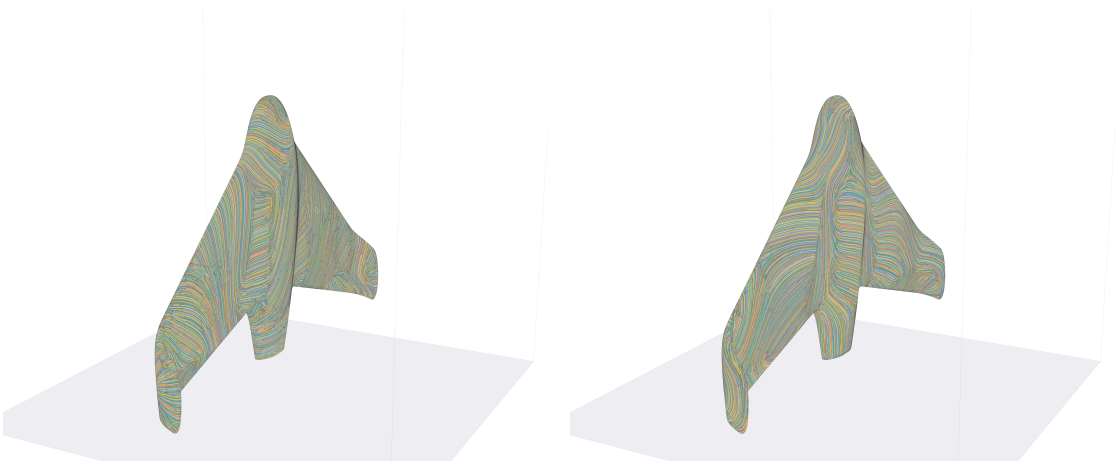
The reported dome ratio corresponds to the adopted through-thickness allowable Z_t, zero out-of-plane normal-interaction coefficients $f^*_{13} = f^*_{23} = 0$, and a fixed structural solution. Both wing frame indices lie well below the Tsai–Wu reference value of 1. A check at 1.5 and 1.0 mm structural mesh resolution changes each ratio by less than $0.1\,\%$ and preserves the ordering. The fixed-stress result is case dependent: the conformal-frame 99th-percentile Tsai–Wu index is substantially lower for the dome, while one tested planar frame is slightly lower for the wing.

6.8. Computational workflow and intended use

The synthesis of mechanics, conformal geometry, path generation, finite-width realization, and evaluation is a central contribution of this study. It is embodied in an inspectable computational workflow for structural designers, toolpath and computer-aided manufacturing (CAM) developers, and multi-axis manufacturing engineers. The workflow links product geometry and loading to a supplied stress field, stress-aligned path generation, and a finite-width toolpath proposal. Before fabrication, users can inspect its coverage, overlap, alignment, and stress context to judge whether it merits machine planning and physical testing. The output is a set of geometric deposition paths for subsequent machine-command ordering.

6.8.1. Complex-geometry demonstrator

The separate monobody unmanned aerial vehicle (UAV) example in Figure 13 applies the geometry-to-path stages to a more product-like shell. The surface combines a blended centre body, swept wings, winglets, and two tail-wall loops. The major and minor renders show the finite-width layouts produced on this more product-like geometry. This demonstrator is outside the five-case structural evaluation.



(a) major alignment **(b)** minor alignment

Figure 13: Computational finite-width path demonstrator on the monobody UAV outer shell. Colours distinguish adjacent ribbons for visual inspection and carry no scalar value or cross-panel identity. The unscaled shell spans 401 mm, compared with the nominal 400 mm build cube.

6.9. Answers to the research questions

Table 12 links each operational research question to the evidence used and the resulting answer.

Table 12: Evidence used to answer the operational research questions.

RQ	Evidence	Answer
RQ1	five-case geometric results (Table 6 and Figure 12), complete-pipeline comparison (Table 8), and solver-start sensitivity (Table 10)	a spectral direction field converts the principal-stress line field into a phase whose level sets are extracted as centrelines and assigned the prescribed bead width. At the reported trace-mesh resolution, the fifteen recorded realizations fell below the separate coverage, overlap, and directional-error reference values; the solver-start check shows that exact path placement remains sensitive at this resolution
RQ2	path-dependent fixed-stress formulation and unmodified-setting verification (Chapter 5), with the equal-area coverage-defect comparison (Table 9)	the realized path defines the local material axes, the local coverage fraction reduces the in-plane allowables, and bead ends apply the endpoint stress factor. The equal-area test applies the same zero-coverage perturbation at two locations. Under the capped stress-magnitude control, their readings become similar, indicating that stress magnitude is a principal contributor to the observed two-site contrast. The resulting index level is interpreted comparatively
RQ3	path-free material-frame comparison on the wing and end dome (Table 11), checked at two structural resolutions	the end dome gives a lower conformal-frame 99th-percentile Tsai–Wu index within the test, whereas the small wing difference cannot establish a planar advantage because one conformal frame is compared with the lowest-index member of the thirteen-normal planar set

RQ1 concerns the complete path-generation pipeline and reports missing deposition, repeated deposition, and directional deviation individually. RQ2 then evaluates a realized path under fixed stress and retains the stress level at each defect location. RQ3 isolates the material-frame comparison by removing the realized path.

Taken together, the three answers support the overarching question at the level of initial computational feasibility for the material and deposition process studied. The computational workflow is the practical result of this synthesis: it connects a thin-shell load case to finite-width conformal paths and an inspectable evaluation before fabrication.

These findings also clarify how the study relates to prior work. The comparison of complete path-generation pipelines applies the periodic scalar-field approach used for stress-guided spatial fibre paths (Zhang et al., 2025), while treating extraction and finite-width realization as part of the evaluated pipeline. The equal-area synthetic-defect comparison complements objectives that address manufacturability during path generation (Yang et al., 2025; Zmyślony et al., 2025) by relating defects in a realized path to a fixed local stress context. The path-free material-frame comparison isolates frame effects under fixed stress. Variable-stiffness optimization instead re-solves the structural problem as material orientation changes (Brampton et al., 2015; Jiang et al., 2019).

6.10. Limitations

- **Simulation and calibration.** The study is computational, and J_{mfg}^{p99} is interpreted as a comparative index. Calibration on printed shells is needed before predictive

use and should quantify parameter interactions and material uncertainty. The effective material card comes from straight deposited specimens and may overstate directional benefit at turns, joins, and terminations (Ye et al., 2025).

- **Forward, fixed-stress scope.** The isotropic shell represents the full wall through its total thickness, while each alignment input is generated and evaluated independently using the mid-plane membrane stress. A predictive layer-stack study would assemble and re-solve the deposited laminate and recover the local outer-surface bending demand.
- **Numerical discretization.** The paths and derived measures are reported at the stated structural- and trace-mesh resolutions. Establishing convergence requires a refinement study and a quantified rule for selecting among admissible spectral modes. The end-dome solver-start check demonstrates sensitivity at the reported trace resolution; the retained diagnostics cannot separate the contributions of eigenspace clustering, mesh resolution, and the ill-conditioned target field.
- **Surface lookup and boundary treatment.** The geometric queries use Euclidean proximity, which can associate folded regions that are close in space but far apart along the surface. The tangent-plane coverage calculation retains all sixteen ring points at an open boundary under the same lookup rule. Intrinsic surface lookup and a boundary-specific sensitivity test are needed to quantify these effects on the 99th-percentile value.
- **Scope of the examples.** The evidence consists of five procedurally defined geometries with prescribed load cases. The path-free material-frame comparison covers two of those geometries and thirteen prescribed planar directions.
- **Manufacturing scope.** The workflow ends at a geometric path proposal. Machine planning must still address collision-free five-axis motion, extrusion control, starts, stops, travel, seams, and retractions. Physical testing must address thermal effects, printability, substrate fabrication, and release. Concave geometries such as the S-bend duct and prosthetic-socket interior also require an access strategy. The overlap measure ρ_o reports local over-deposition and z-height accumulation separately from the fixed-stress index. Adaptive widths are modelled ribbon widths; qualifying them requires process-specific extrusion limits. The candidate substrates require body-integrity and self-intersection checks before fabrication.

7

Conclusion and future work

We developed and evaluated a computational prototype for materials whose deposited properties depend on path direction, using short-fibre FFF as the first practical case. The central contribution is an inspectable computational workflow that synthesizes a fixed shell stress field, conformal surface construction, spectral direction-field path generation, finite-width bead realization, and path-dependent fixed-stress evaluation. It carries the mechanical intent of a thin-shell load case through to geometric paths that can be inspected before machine planning and physical testing.

For RQ1, the fifteen recorded path realizations across the five shell geometries fell below the contextual coverage, overlap, and directional-error reference values at the trace-mesh resolution used in the study. Among these fifteen, the maximum reported directional error, 3.74°, was below the contextual 5° reference value. In the comparison of complete path-generation pipelines, every reported spectral direction field row was below the common coverage and overlap reference values and below the directional reference value for its transferred target. The streamline rows exceeded the adopted coverage-shortfall reference value. The single row for harmonic scalar contouring remained below the coverage reference value but exceeded both the overlap reference value and, against its own smoothed target, the directional reference value.

A supplemental three-seed end-dome sensitivity check changed only the eigensolver starting vector within a matched numerical configuration. It produced different bead sets and derived measures, including one major-input directional-error value above the contextual 5° reference value. The five-case result is therefore a report of the recorded paths at the stated resolution, while exact path placement remains numerically unresolved.

For RQ2, the local index I_{mfg} formulates coverage shortfall, misalignment, and bead discontinuity in their fixed-stress context, and J_{mfg}^{p99} is the physical-area-weighted 99th percentile of the local index. The equal-area comparison applied the same modelled zero-coverage perturbation at two locations. The higher-stress site received the larger mean local index. The capped stress-magnitude control made the readings similar and reversed the small residual difference, indicating that stress magnitude is a principal contributor to the observed two-site contrast.

For RQ3, the path-free material-frame comparison held the stress fixed and changed only the material axes. The conformal-frame 99th-percentile Tsai–Wu index was substantially lower on the end dome. On the wing, the lowest of thirteen prescribed planar-frame indices was slightly lower than the single conformal-frame index. Because this one-versus-thirteen comparison reports the minimum planar value, the small wing difference is inconclusive. The comparison is therefore a case-dependent fixed-stress material-frame sensitivity.

Together, these results support initial computational feasibility for the workflow in short-fibre FFF. The prototype translated thin-shell load fields into finite-width conformal path proposals and, before fabrication, evaluated the modelled effects of coverage shortfall, misalignment, and bead discontinuity under a fixed stress field. As a separate geometry-to-path demonstration, the monobody UAV example produced inspectable major- and minor-input layouts on a complex product-like shell.

7.1. Future work

The next computational step is to establish structural- and trace-mesh convergence and quantify the stability of the generalized eigenvalue solution. The trace mesh should be refined through the $w/2$ resolution target, with eigenvalues, eigenpair residuals, and eigenvectors stored. Global sign and phase should be aligned before comparing modes, and nearby eigenspaces compared as subspaces. Subspace tracking, a block eigensolver, and a consistent rule for choosing among nearby modes should then be tested. Same-seed repeats would test numerical repeatability; the same varied-seed set at each resolution would diagnose starting-vector sensitivity. Geometric lookups should follow mesh connectivity or intrinsic surface distance where regions are close in space but distant along the surface.

Physical calibration is the next empirical step. Matched coupons should measure the effects of coverage shortfall, misalignment, and bead discontinuity under the intended material and process conditions. Those data would replace the uncalibrated literature-informed relations in I_{mfg}, determine whether J_{mfg}^{p99} predicts observed damage, and establish whether it can become a starting framework for quantitative structural assessment after printed-shell validation and structural re-solving.

Complete-laminate evaluation should generate all intended layer toolpaths, assemble them into a laminate model, and re-solve multiple load cases for membrane, bending, free-edge, and interlayer effects. This could support an alignment schedule rather than the independent path-realization sensitivities reported here.

A subsequent comparison should assess the conformal shell-and-path strategy against sparse infill under matched outer geometry, material mass, loads, and process assumptions, comparing their structural and manufacturing performance.

The manufacturing step is to convert the conformal paths into collision-free five-axis motion with controlled orientation, travel, extrusion, and substrate interaction, followed by a printed demonstrator and mechanical testing. Transferring the workflow to continuous-fibre or other feedstocks whose properties depend on deposition direction would also require explicit steering-radius, tow continuity, compaction, and material-specific constraints.

Bibliography

Barbero, E. J. (2018). *Introduction to composite materials design* (3rd). CRC Press.

Batoz, J.-L., Bathe, K.-J., & Ho, L.-W. (1980). A study of three-node triangular plate bending elements. *International Journal for Numerical Methods in Engineering*, *15*(12), 1771–1812. https://doi.org/10.1002/nme.1620151205

Bendsøe, M. P., Guedes, J. M., Haber, R. B., Pedersen, P., & Taylor, J. E. (1994). An analytical model to predict optimal material properties in the context of optimal structural design. *Journal of Applied Mechanics*, *61*(4), 930–937. https://doi.org/10.1115/1.2901581

Bommes, D., Lévy, B., Pietroni, N., Puppo, E., Silva, C., Tarini, M., & Zorin, D. (2013). Quad-mesh generation and processing: A survey. *Computer Graphics Forum*, *32*(6), 51–76. https://doi.org/10.1111/cgf.12014

Bommes, D., Zimmer, H., & Kobbelt, L. (2009). Mixed-integer quadrangulation. *ACM Transactions on Graphics*, *28*(3), Article 77. https://doi.org/10.1145/1531326.1531383

Brampton, C. J., Wu, K. C., & Kim, H. A. (2015). New optimization method for steered fiber composites using the level set method. *Structural and Multidisciplinary Optimization*, *52*(3), 493–505. https://doi.org/10.1007/s00158-015-1256-6

Brenken, B., Barocio, E., Favaloro, A., Kunc, V., & Pipes, R. B. (2018). Fused filament fabrication of fiber-reinforced polymers: A review. *Additive Manufacturing*, *21*, 1–16. https://doi.org/10.1016/j.addma.2018.01.002

Chakraborty, D., Reddy, B. A., & Roy Choudhury, A. (2008). Extruder path generation for curved layer fused deposition modeling. *Computer-Aided Design*, *40*(2), 235–243. https://doi.org/10.1016/j.cad.2007.10.014

Chen, X., Fang, G., Liao, W.-H., & Wang, C. C. L. (2022). Field-based toolpath generation for 3D printing continuous fibre reinforced thermoplastic composites. *Additive Manufacturing*, *49*, Article 102470. https://doi.org/10.1016/j.addma.2021.102470

Chermain, X., Cocco, G., Zanni, C., Garner, E., Hugron, P.-A., & Lefebvre, S. (2025). Atomizer: Beyond non-planar slicing for fused filament fabrication. *Computer Graphics Forum*, *44*(5), Article e70189. https://doi.org/10.1111/cgf.70189

Clarke, T., & Hosseini, A. (2025). Enhancing yield prediction of FFF materials with modified Tsai–Wu failure criterion. *The International Journal of Advanced Manufacturing Technology*, *141*(7–8), 3737–3758. https://doi.org/10.1007/s00170-025-16785-0

Cocco, G., Belle, V., Garner, E., Lefebvre, S., & Chermain, X. (2026). AtomSlicer: Constant-thickness field-aligned non-planar slicing and continuous toolpaths for FFF. *ACM Transactions on Graphics*, *45*(4). https://doi.org/10.1145/3811363

Cocco, G., & Chermain, X. (2026). Field-aligned surface-filling curve via implicit stitching. *Computer Graphics Forum*, Article e70361. https://doi.org/10.1111/cgf.70361

Crane, K., Desbrun, M., & Schröder, P. (2010). Trivial connections on discrete surfaces. *Computer Graphics Forum*, *29*(5), 1525–1533. https://doi.org/10.1111/j.1467-8659.2010.01761.x

Crane, K., Weischedel, C., & Wardetzky, M. (2013). Geodesics in heat: A new approach to computing distance based on heat flow. *ACM Transactions on Graphics*, *32*(5), 152:1–152:11. https://doi.org/10.1145/2516971.2516977

Dai, C., Wang, C. C. L., Wu, C., Lefebvre, S., Fang, G., & Liu, Y.-J. (2018). Support-free volume printing by multi-axis motion. *ACM Transactions on Graphics*, *37*(4), Article 134. https://doi.org/10.1145/3197517.3201342

Daniel, I. M., & Ishai, O. (2006). *Engineering mechanics of composite materials* (2nd ed.). Oxford University Press.

Fang, G., Zhang, T., Huang, Y., Zhang, Z., Masania, K., & Wang, C. C. L. (2024). Exceptional mechanical performance by spatial printing with continuous fiber: Curved slicing, toolpath generation and physical verification. *Additive Manufacturing*, *82*, Article 104048. https://doi.org/10.1016/j.addma.2024.104048

Fang, G., Zhang, T., Zhong, S., Chen, X., Zhong, Z., & Wang, C. C. L. (2020). Reinforced FDM: Multi-axis filament alignment with controlled anisotropic strength. *ACM Transactions on Graphics*, *39*(6), Article 204. https://doi.org/10.1145/3414685.3417834

Goh, G. D., Yap, Y. L., Agarwala, S., & Yeong, W. Y. (2019). Recent progress in additive manufacturing of fiber reinforced polymer composite. *Advanced Materials Technologies*, *4*(1), Article 1800271. https://doi.org/10.1002/admt.201800271

Guidetti, X., Balta, E. C., Nagel, Y., Yin, H., Rupenyan, A., & Lygeros, J. (2023). Stress flow guided non-planar print trajectory optimization for additive manufacturing of anisotropic polymers. *Additive Manufacturing*, *72*, Article 103628. https://doi.org/10.1016/j.addma.2023.103628

Guo, Y., Pradhan, A., Jonson, P., & Boddeti, N. (2025). Design and additive manufacture of architected short fiber reinforced composites. *Applied Research*, *4*(3), Article e70020. https://doi.org/10.1002/appl.70020

Gürdal, Z., & Olmedo, R. (1993). In-plane response of laminates with spatially varying fiber orientations: Variable stiffness concept. *AIAA Journal*, *31*(4), 751–758. https://doi.org/10.2514/3.11613

Hashin, Z. (1980). Failure criteria for unidirectional fiber composites. *Journal of Applied Mechanics*, *47*(2), 329–334. https://doi.org/10.1115/1.3153664

Hedgepeth, J. M. (1961). *Stress concentrations in filamentary structures* (tech. rep. No. NASA TN D-882). NASA Langley Research Center.

IJsselmuiden, S. T., Abdalla, M. M., & Gürdal, Z. (2008). Implementation of strength-based failure criteria in the lamination parameter design space. *AIAA Journal*, *46*(7), 1826–1834. https://doi.org/10.2514/1.35565

Jacquemet, V. (2024). Improved algorithm for generating evenly-spaced streamlines from an orientation field on a triangulated surface. *Computer Methods and Programs in Biomedicine*, *251*, Article 108202. https://doi.org/10.1016/j.cmpb.2024.108202

Jiang, D., Hoglund, R., & Smith, D. E. (2019). Continuous fiber angle topology optimization for polymer composite deposition additive manufacturing. *Fibers*, *7*(2), Article 14. https://doi.org/10.3390/fib7020014

Jobard, B., & Lefer, W. (1997). Creating evenly-spaced streamlines of arbitrary density. *Visualization in Scientific Computing '97*, 43–55. https://doi.org/10.1007/978-3-7091-6876-9_5

Kipping, J., & Schüppstuhl, T. (2023). Load-oriented nonplanar additive manufacturing method for optimized continuous carbon fiber parts. *Materials*, *16*(3), Article 998. https://doi.org/10.3390/ma16030998

Knöppel, F., Crane, K., Pinkall, U., & Schröder, P. (2013). Globally optimal direction fields. *ACM Transactions on Graphics*, *32*(4), Article 59. https://doi.org/10.1145/2461912.2462005

Knöppel, F., Crane, K., Pinkall, U., & Schröder, P. (2015). Stripe patterns on surfaces. *ACM Transactions on Graphics*, *34*(4), Article 39. https://doi.org/10.1145/2767000

Knudsen, F. P. (1959). Dependence of mechanical strength of brittle polycrystalline specimens on porosity and grain size. *Journal of the American Ceramic Society*, *42*(8), 376–387. https://doi.org/10.1111/j.1151-2916.1959.tb13596.x

Li, X., Liu, W., Hu, Z., He, C., Ding, J., Chen, W., Wang, S., & Dong, W. (2024). Supportless 3D-printing of non-planar thin-walled structures with the multi-axis screw-extrusion additive manufacturing system. *Materials & Design*, *240*, Article 112860. https://doi.org/10.1016/j.matdes.2024.112860

Liu, G., Huang, W., Wang, Y., Ren, H., Zhang, G., Zhou, L., & Xiong, Y. (2024). Stress field-aware infill toolpath generation for additive manufacturing of continuous fiber reinforced polymer composites. *Materials & Design*, *239*, Article 112756. https://doi.org/10.1016/j.matdes.2024.112756

Liu, T., Zhang, T., Chen, Y., Huang, Y., & Wang, C. C. L. (2024). Neural slicer for multi-axis 3D printing. *ACM Transactions on Graphics*, *43*(4), Article 85. https://doi.org/10.1145/3658212

Liu, T., Yuan, S., Wang, Y., Xiong, Y., Zhu, J., Lu, L., & Tang, Y. (2023). Stress-driven infill mapping for 3D-printed continuous fiber composite with tunable infill density and morphology. *Additive Manufacturing*, *62*, Article 103374. https://doi.org/10.1016/j.addma.2022.103374

Lupone, F., Padovano, E., Venezia, C., & Badini, C. (2022). Experimental characterization and modeling of 3D printed continuous carbon fibers composites with different fiber orientation produced by FFF process. *Polymers*, *14*(3), Article 426. https://doi.org/10.3390/polym14030426

Mehdikhani, M., Gorbatikh, L., Verpoest, I., & Lomov, S. V. (2019). Voids in fiber-reinforced polymer composites: A review on their formation, characteristics, and effects on mechanical performance. *Journal of Composite Materials*, *53*(12), 1579–1669. https://doi.org/10.1177/0021998318772152

Pedersen, P. (1989). On optimal orientation of orthotropic materials. *Structural Optimization*, *1*(2), 101–106. https://doi.org/10.1007/BF01637666

Pedersen, P. (1990). Bounds on elastic energy in solids of orthotropic materials. *Structural Optimization*, *2*(1), 55–63. https://doi.org/10.1007/BF01743521

Pilkey, W. D., & Pilkey, D. F. (2008). *Peterson's stress concentration factors* (3rd). John Wiley & Sons. https://doi.org/10.1002/9780470211106

Pinho, S. T., Iannucci, L., & Robinson, P. (2006). Physically based failure models and criteria for laminated fibre-reinforced composites with emphasis on fibre kinking. Part I: Development. *Composites Part A: Applied Science and Manufacturing*, *37*(1), 63–73. https://doi.org/10.1016/j.compositesa.2005.04.016

Puck, A., & Schürmann, H. (2002). Failure analysis of FRP laminates by means of physically based phenomenological models. *Composites Science and Technology*, *62*(12–13), 1633–1662. https://doi.org/10.1016/S0266-3538(01)00208-1

Ray, N., Li, W. C., Lévy, B., Sheffer, A., & Alliez, P. (2006). Periodic global parameterization. *ACM Transactions on Graphics*, *25*(4), 1460–1485. https://doi.org/10.1145/1183287.1183297

Sales, E., Kwok, T.-H., & Chen, Y. (2021). Function-aware slicing using principal stress line for toolpath planning in additive manufacturing. *Journal of Manufacturing Processes*, *64*, 1420–1433. https://doi.org/10.1016/j.jmapro.2021.02.050

Seharing, A., Azman, A. H., & Abdullah, S. (2020). A review on integration of lightweight gradient lattice structures in additive manufacturing parts. *Advances in Mechanical Engineering*, *12*(6), 1687814020916951. https://doi.org/10.1177/1687814020916951

Setoodeh, S., Gürdal, Z., & Watson, L. T. (2006). Design of variable-stiffness composite layers using cellular automata. *Computer Methods in Applied Mechanics and Engineering*, *195*(9–12), 836–851. https://doi.org/10.1016/j.cma.2005.03.005

Spriggs, R. M. (1961). Expression for effect of porosity on elastic modulus of polycrystalline refractory materials, particularly aluminum oxide. *Journal of the American Ceramic Society*, *44*(12), 628–629. https://doi.org/10.1111/j.1151-2916.1961.tb11671.x

Sun, B., Mubarak, S., Zhang, G., Peng, K., Hu, X., Zhang, Q., Wu, L., & Wang, J. (2023). Fused-Deposition Modeling 3D printing of short-cut carbon-fiber-reinforced PA6 composites for strengthening, toughening, and light weighting. *Polymers*, *15*(18), Article 3722. https://doi.org/10.3390/polym15183722

Tam, K.-M. M., & Mueller, C. T. (2017). Additive manufacturing along principal stress lines. *3D Printing and Additive Manufacturing*, *4*(2), 63–81. https://doi.org/10.1089/3dp.2017.0001

Taubin, G. (1995). Curve and surface smoothing without shrinkage. *Proceedings of the Fifth International Conference on Computer Vision*, 852–857. https://doi.org/10.1109/ICCV.1995.466848

Tekinalp, H. L., Kunc, V., Velez-Garcia, G. M., Duty, C. E., Love, L. J., Naskar, A. K., Blue, C. A., & Ozcan, S. (2014). Highly oriented carbon fiber–polymer composites via additive manufacturing. *Composites Science and Technology*, *105*, 144–150. https://doi.org/10.1016/j.compscitech.2014.10.009

Tsai, S. W., & Hahn, H. T. (1980). *Introduction to composite materials*. Technomic Publishing.

Tsai, S. W., & Wu, E. M. (1971). A general theory of strength for anisotropic materials. *Journal of Composite Materials*, *5*(1), 58–80. https://doi.org/10.1177/002199837100500106

Turner, M. J., Clough, R. W., Martin, H. C., & Topp, L. J. (1956). Stiffness and deflection analysis of complex structures. *Journal of the Aeronautical Sciences*, *23*(9), 805–823. https://doi.org/10.2514/8.3664

Vannucci, P., & Verchery, G. (2001). Stiffness design of laminates using the polar method. *International Journal of Solids and Structures*, *38*(50–51), 9281–9294. https://doi.org/10.1016/S0020-7683(01)00177-9

Vaxman, A., Campen, M., Diamanti, O., Panozzo, D., Bommes, D., Hildebrandt, K., & Ben-Chen, M. (2016). Directional field synthesis, design, and processing. *Computer Graphics Forum*, *35*(2), 545–572. https://doi.org/10.1111/cgf.12864

Wang, J., Liu, Y., Wu, J., & Westermann, R. (2026). Topology-aware stress analysis in shell structures. *Computer Methods in Applied Mechanics and Engineering*, *452*, Article 118770. https://doi.org/10.1016/j.cma.2026.118770

Wu, J., Aage, N., Westermann, R., & Sigmund, O. (2018). Infill optimization for additive manufacturing—approaching bone-like porous structures. *IEEE Transactions on Visualization and Computer Graphics*, *24*(2), 1127–1140. https://doi.org/10.1109/TVCG.2017.2655523

Yang, Y., Xu, Z., & Duan, M. (2025). Evolving stress-guided continuous fiber path optimization for multi-axis additive manufacturing of composite shells. *Additive Manufacturing*, *113*, Article 105012. https://doi.org/10.1016/j.addma.2025.105012

Ye, Y., Yang, Z., Qu, D., Hu, B., & Li, L. (2025). Orthotropic constitutive modeling and Tsai–Wu failure criterion for carbon fiber-reinforced PEEK composites. *Polymers*, *17*(8), Article 1076. https://doi.org/10.3390/polym17081076

Zhang, T., Fang, G., Huang, Y., Dutta, N., Lefebvre, S., Kilic, Z. M., & Wang, C. C. L. (2022). S^3-slicer: A general slicing framework for multi-axis 3D printing. *ACM Transactions on Graphics*, *41*(6), Article 277. https://doi.org/10.1145/3550454.3555516

Zhang, T., Liu, T., Dutta, N., Chen, Y., Su, R., Zhang, Z., Wang, W., & Wang, C. C. L. (2025). Toolpath generation for high density spatial fiber printing guided by principal stresses. *Composites Part B: Engineering*, *295*, Article 112154. https://doi.org/10.1016/j.compositesb.2025.112154

Zmyślony, M., Dradrach, K., & Biggins, J. S. (2025). Slicing vector fields into tool paths for additive manufacturing of nematic elastomers. *Additive Manufacturing*, *97*, Article 104604. https://doi.org/10.1016/j.addma.2024.104604

Disclosure of AI use

OpenAI Codex and Anthropic Claude Code were used as computer-assisted tools during this project. Their roles included reviewing and debugging Python and C++ code; assisting with the integration of open-source codebases; assisting with literature searches and source checking; discussing and refining research ideas and validation methods; and improving the structure and language of the report.

Numerical results reported here were produced by the project code and result files, not estimated by a language model. AI-generated suggestions were treated as unverified until checked against executable tests, primary literature, or the source simulation output. No generative-AI image is used as scientific evidence in this report; the figures are plots, diagrams, or renders derived from the project data and geometry. The author retains responsibility for the research decisions, interpretations, source use, and final submitted text.